

VoxelPrompt: A Vision-Language Agent for Grounded Medical Image Analysis

Andrew Hoopes^{1,2}, Victor Ion Butoi¹, John V. Guttag¹, Adrian V. Dalca^{1,2,3}

1. Massachusetts Institute of Technology, 2. Massachusetts General Hospital, 3. Harvard Medical School

We present VoxelPrompt, an agent-driven vision-language framework that tackles diverse radiological tasks through joint modelling of natural language, image volumes, and analytical metrics. VoxelPrompt is multi-modal and versatile, leveraging the flexibility of language interaction while providing quantitatively grounded image analysis. Given a variable number of 3D medical volumes, such as MRI and CT scans, VoxelPrompt employs a language agent that iteratively predicts executable instructions to solve a task specified by an input prompt. These instructions communicate with a vision network to encode image features and generate volumetric outputs (e.g., segmentations). VoxelPrompt interprets the results of intermediate instructions and plans further actions to compute discrete measures (e.g., tumor growth across a series of scans) and present relevant outputs to the user. We evaluate this framework in a sandbox of diverse neuroimaging tasks, and we show that the single VoxelPrompt model can delineate hundreds of anatomical and pathological features, measure many complex morphological properties, and perform open-language analysis of lesion characteristics. VoxelPrompt carries out these objectives with accuracy similar to that of fine-tuned, single-task models for segmentation and visual question-answering, while facilitating a much larger range of tasks. Therefore, by supporting accurate image processing with language interaction, VoxelPrompt provides comprehensive utility for numerous imaging tasks that traditionally require specialized models to address.

Keywords: Vision-Language Agent, Medical Image Analysis, Neuroimage Foundation Model

1 Introduction

Automated methods for medical image analysis increasingly use learning-based techniques to address clinical and research aims. Typically, these methods are tailored to a narrow set of computational objectives and output modalities (e.g. domain-specific segmentations, classification of tumors, or natural language characterizations). This specialization limits the broad use of deep-learning advancements in radiology, by forcing clinicians and researchers to navigate a fragmented collection of inflexible tools – often failing to find one that meets their need.

For example, a practitioner might need to analyze the growth of a specific tumor in a patient exhibiting multiple lesions and abnormalities. While many tumor segmentation models exist, none enable the user to easily specify and differentiate the desired pathology, for instance, based on descriptors such as relative location, size, or signal intensity. Moreover, these methods rarely extend to cover the downstream computational steps required to extract meaningful analytical metrics. This ultimately leaves the burden of task-specific post-processing to the users.

In this work, we present a mechanism that supports a *unified* medical imaging model, capable of conducting interactive, end-to-end analysis across a spectrum of goals. We introduce VoxelPrompt, a system that, in response to a text prompt, processes volumetric (3D) medical scans

and outputs varied modalities, including language, volumes, and computed metrics. With this system, a single model can learn to localize precise anatomical and pathological regions of interest (ROIs), carry out complex computational measurements that relate multiple scans to one another, and perform open-language characterization of image features (Figure 1).

VoxelPrompt features an image encoder, image generator, and language model, all trained jointly. The language model functions as a planning agent, iteratively predicting instructions as executable code and interpreting its outcomes to achieve a target goal. The dynamically-evaluated instructions orchestrate the encoding and generation of spatial features (e.g., segmentations), incorporate natural language responses, and access a predefined library of functions to compute and provide outputs to the user.

We implement an instructable convolutional network that integrates language model embeddings to promote fine-grained, language-conditioned visual analysis. This vision network includes attention-based interaction of features across a volume sequence of *any length* to accommodate adaptive analysis in multi-acquisition and longitudinal scenarios. Unlike typical volumetric processing models, which are largely restricted to a fixed number of image channels and voxel spacing, VoxelPrompt supports a variable number of inputs and performs convolutions in the native acquisition resolution.

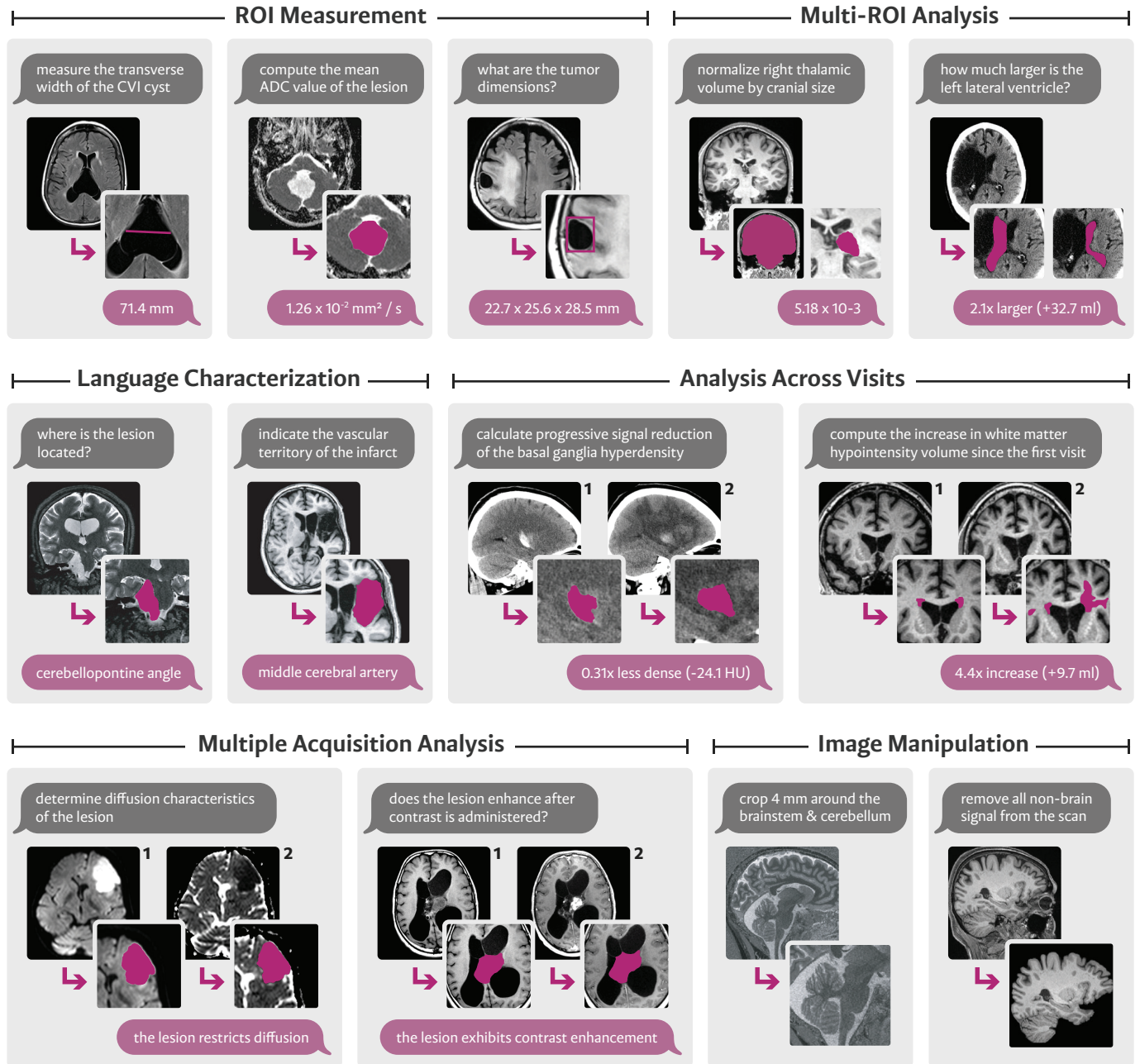


Figure 1. Examples from the diverse set of tasks supported by the VoxelPrompt framework. For each example, we show the input prompt (gray) above the input image(s). VoxelPrompt annotates the images and generates language responses (shown in purple). These scans are processed entirely in 3D, but here we show only a single extracted slice.

We evaluate the capability of the VoxelPrompt system to support end-to-end, multi-modal analysis using a handcrafted set of diverse brain-imaging tasks, covering a wide range of MRI and CT acquisitions, anatomies, and diseases. We demonstrate that the single VoxelPrompt model properly plans and executes the steps necessary to perform these tasks while *also* capturing the individual accuracy of fine-tuned, single-task baselines for brain feature segmentation and pathology-based visual question-answering. Additionally, we show that natural language

offers an effective mechanism for flexible model interaction. VoxelPrompt aligns descriptive text with image features to target hundreds of anatomical and pathological ROIs, and it properly considers descriptive factors such as spatial and signal characteristics.

We focus this work in brain image analysis – a large field with crucial impact in neurology. However, we design VoxelPrompt to be broadly applicable across medical domains, and we hope it provides a technical framework for future development of universal radiology utilities.

2 Related Work

2.1 Brain Region Analysis

In neuroimaging, interpreting and analyzing ROI characteristics is central to clinical decision-making as well as understanding brain structure, function, and development. To support these aims, widely-used processing pipelines typically employ algorithms that delineate relevant features and quantify their size, shape, connectivity, composition, and change over time [1–7].

Modern processing methods train deep-learning architectures to segment diverse anatomy and pathology, such as subcortical and cortical structures [8–13], cerebral vessels [14, 15], white matter tracts [16–18], tumors [19–22], intracranial hemorrhages [23], ischemic stroke [24–26], and various other lesions [27–29]. Specialized for individual applications, these tools generally output only fixed segmentation targets and require significant human involvement in their use for analyzing data and deriving downstream ROI measures. Alternative learning-based approaches enable the direct estimation of image characterizations – such as tumor classification [30, 31], brain age [32–34], and dementia scores [35–38] – without the need for intermediate ROI processing.

2.2 Learning Across Medical Imaging Tasks

Recent methods in medical image analysis consolidate multiple objectives within a *single* framework and build on multi-task learning techniques [39–41]. These approaches aim to improve performance, generalization, and training efficiency by exploiting shared representations across diverse segmentation, classification, registration, and statistical modelling objectives [42–46].

Adaptable multi-task models learn to address specific tasks at inference with user-provided support. For instance, interactive segmentation tools can adapt to specific biomedical targets, prompted by partial image annotations [47–51]. Similarly, few-shot and in-context learning methods [52, 53], which leverage a set of example input-output image pairs as guidance, can generalize to medical segmentation [54–57] and broad neuroimaging tasks [58] without model fine-tuning. Task-query mechanisms offer robust test-time versatility, but creating support data for each analysis can be challenging and impractical. Overall, these multi-task models are developed as either pretraining or specialized methods that do not aim to address a complete analytical pipeline.

2.3 Medical Vision-Language Models

Vision-language models (VLMs) learn joint representations of images and text to facilitate language-driven image analysis. They often combine language models with image encoders, aligning visual and text features with

contrastive learning techniques [59]. Using large-scale biomedical image-caption datasets [60–63], generalized VLM pretraining can facilitate downstream fine-tuning (and even zero-shot or few-shot performance) for visual question answering tasks in medical imaging [61, 63–79]. More specialized language-generating medical VLMs focus on individual aims, such as the estimation of clinical reports directly from images [80–90]. However, with the exception of few recent works [64, 65, 77, 91, 92], most general-domain models are trained exclusively on two-dimensional image slices, often X-rays, making them inappropriate for standard 3D MR and CT imaging.

Alternatively, image-generating medical VLMs incorporate text embeddings into vision networks to develop promptable biomedical segmenters [93–95] or generators of scans with user-specified characteristics [96–98]. Augmented training schemes use text as additional supervision for improving pathology segmentation [65] or localization [99], but these do not focus on using or generating language at inference time. Recent work introduces a question-answering VLM that generates both language, for image characterization, and conditional segmentations for a predefined set of image targets [92].

2.4 Language Models as Agents

Building on the code-prediction and chain-of-thought capabilities of large language models [100–103], recent work beyond the medical domain trains text generating networks as intelligent agents that plan and execute actions to solve a prescribed computational task. Agents call on external APIs to address problems that require more than natural language prediction, such as mathematical computation [104, 105], image analysis [106–109], web interaction [110–112], scientific discovery [113, 114], and general-domain task solving [115, 116].

Adaptive, or feedback-driven, agents manage complex problems with unpredictable dynamics by making planning decisions based on observed outcomes of intermediate actions [117–122]. Instead of predicting an entire action sequence at once, these adaptive agents follow an iterative, step-wise process of planning, executing, and interpreting an action’s effect within an environment. In VoxelPrompt, we build on these ideas to implement an adaptive agent that interacts with a library of processing functions and instructs image volume encoding and generation through jointly-learned vision networks.

A recent contemporaneous method [123] trains a language model to address a discrete set of medical imaging goals by selecting and executing pretrained, task-specific tools. Unlike VoxelPrompt, this model does not execute downstream operations to extract key metrics and does not leverage the flexibility of language prompting for distinguishing nuanced ROIs with desired characteristics.

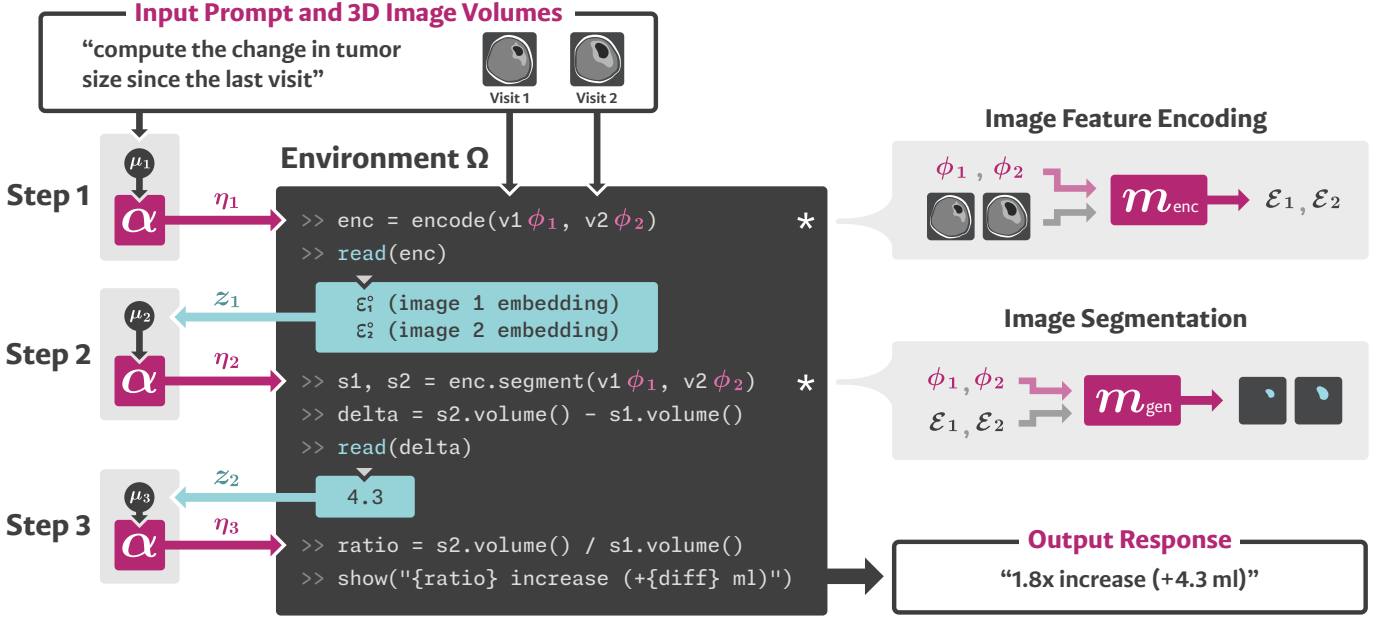


Figure 2. To solve a language-prompted task, the adaptive agent model α outputs instructions η as code to run in a persistent execution environment Ω . Across multiple steps, the agent interprets execution outcomes z (blue) to guide subsequent instruction prediction. To perform vision operations, such as volume encoding or generation, α can instruct the execution of vision networks m_{enc} and m_{gen} , which are manipulated by image-specific latent instruction embeddings ϕ .

3 Method

We design a vision-language instruction system that processes a set of medical image volumes \mathcal{V} based on an input text prompt p (Figure 2). To address the task defined by p , a language-model-based agent α outputs instructions η , which include code executed in an environment Ω . This code calls functions from a predefined library to perform actions such as mathematical computation, user-interface interaction, volume interpretation, and segmentation. Various volume operations are enabled by a vision encoder m_{enc} and generator m_{gen} , which are jointly trained with α .

Feedback-Driven Instruction. The agent α prepares instructions over several iterative steps, guided by outcomes of previously executed actions. In step i , the agent computes an instruction embedding sequence $\eta_i = \alpha(\mu_i)$, using an input state representation $\mu_i \in \mathbb{R}^{\ell, d}$ with sequence length ℓ and embedding dimension d . We decode η_i into interpretable text φ_i , which we execute as code in Ω .

To initialize the first step, we set μ_1 as the embedded representation of the prompt p and acquisition metadata (such as scan date) for each volume $v \in \mathcal{V}$. In Ω , we predefine a variable corresponding to each v . As the code φ_i is executed, new variables are defined and retained in Ω , which persists across steps. To guide the next instruction step, φ_i can include *read* operations on intermediate variables in Ω . During execution, a *read* operation extracts the value of a variable as interpretable information. We

include the embedded representation z_i of the extracted outputs as feedback in the next state $\mu_{i+1} = \mu_i \parallel \eta_i \parallel z_i$, where \parallel represents sequence dimension concatenation.

This process of instruction planning, execution, and feedback repeats until the task is completed and a stopping instruction is executed.

Vision Network Instruction. Volume encoding and generation functions instruct the execution of m_{enc} and m_{gen} , respectively. Relevant code in φ specifies the variables passed to m_{enc} and m_{gen} , while a set of latent instruction features ϕ , captured in η , modulate the intermediate activations of these networks.

An encoding operation distills \mathcal{V} into sets of features $\mathcal{E} = m_{\text{enc}}(\mathcal{V}, \phi)$. The set \mathcal{E} contains volume-specific encodings \mathcal{E}_v , which have a subset of feature embeddings ε_v^o that are incorporable to z following a *read* function execution. Alternatively, a volume generation operation outputs a set of volumes $\mathcal{W} = m_{\text{gen}}(\mathcal{E}, \phi)$, such as segmentations. In this operation, ϕ might modulate m_{gen} to segment, for example, a particular anatomical target. Volumes \mathcal{W} can be further processed or used by instructions in η to compute downstream, task-specific results.

3.1 Architecture

Language Agent. We implement the agent α using a transformer-based language model architecture. We convert text into the model embedding space by splitting character groups into tokens (from a vocabulary of size γ)

\mathcal{V}	Set of input volumes
p	Input text prompt
α	Agent
m_{enc}	Volume encoder
m_{gen}	Volume generator
\mathcal{E}	Set of volume encodings output by m_{enc}
\mathcal{W}	Set of volumes generated by m_{gen}
Ω	Persistent execution environment
μ	State representation embeddings
η	Instruction embeddings output by α
z	Execution feedback embeddings
φ	Executable code derived from η
ϕ	Manipulation features derived from η
d	Embedding dimension size
γ	Token vocabulary size

Table 1. Summary of key variables defined in the method.

and mapping them to a sequence of \mathbb{R}^d features via an embedding matrix in $\mathbb{R}^{\gamma \times d}$. The model α auto-regressively generates instruction embeddings η based on the input μ . We split η along the sequence-dimension to extract η^φ and η^ϕ . We pass η^ϕ through a fully-connected layer to compute the vision network modulators ϕ . We pass η^φ through a fully-connected layer to obtain text token probabilities $P(\varphi)$, which we decode into φ by choosing the maximum probability token at each sequence position.

Flexible Vision Networks. We implement m_{enc} and m_{gen} as two multi-scale convolutional networks that incorporate ϕ and share information across a flexible number of inputs. We propagate each input volume v through m_{enc} or each volume encoding \mathcal{E}_v through m_{gen} , computing individual *streams* of intermediate activations that interact with each other at intermittent layers.

Specifically, for voxel features $a_s \in \mathbb{R}^c$ in volume stream s , computed by a convolutional layer with c output channels, we concatenate a_s with stream-specific ϕ_s along the channel dimension. We then use a fully-connected layer to yield $a'_s \in \mathbb{R}^c$. At a given spatial location, we stack corresponding voxel representations a'_s across S streams to construct $A' \in \mathbb{R}^{S \times c}$. We interact streams in A' using an attention mechanism with dimension b :

$$B = f(\text{softmax}(QK^T b^{-1/2})V) + A, \quad (1)$$

where $Q, K, V \in \mathbb{R}^{S \times b}$ are linear transformations of A , and fully-connected layer f projects the output to $\mathbb{R}^{S \times c}$. We then separate B back into stream-specific voxel features.

Interpretable Volume Encodings. For each volume v passed through m_{enc} , we reduce the spatial dimensions of the deepest layer output using a global max operator. We pass these pooled features through a fully-connected

layer to compute $\varepsilon_v^\circ \in \mathbb{R}^d$. When a *read* instruction is executed on a set of volume encodings \mathcal{E} defined in Ω , we concatenate each $\varepsilon_v^\circ \in \mathcal{E}$ into the feedback embeddings z .

3.2 Supervised Training

We optimize trainable model parameters θ from scratch using a diverse and carefully curated set of tasks \mathcal{T} (Section 4.1), where θ encompasses the parameters of the language model α and vision networks m_{enc} and m_{gen} . For each task $\tau \in \mathcal{T}$, we predefine target (ground-truth) code φ^* that carries out the task objective. During a training step, we randomly sample $\tau \sim \mathcal{T}$, synthesize a task-specific prompt p , and sample volume inputs \mathcal{V} with ground-truth outputs \mathcal{W}^* , if required. Using these samples at each agent training step, we evaluate the loss:

$$\mathcal{L}_{ce}(P(\varphi), \varphi^*) + \lambda \sum_{j=1}^{|\mathcal{W}|} \mathcal{L}_{img}(\mathcal{W}_j, \mathcal{W}_j^*), \quad (2)$$

where $P(\varphi)$ is output by the language model and volumes \mathcal{W} are generated by the vision networks while executing φ^* . The function \mathcal{L}_{ce} measures cross-entropy between predicted vocabulary probabilities and tokenized target text, and \mathcal{L}_{img} measures differences between a predicted and target image, weighted by a scalar λ . In our experiments, we focus on the most consequential type of intermediate volume for ROI processing – spatial segmentation. Therefore, we set \mathcal{L}_{img} as the soft Dice loss [124].

3.3 Implementation

Development Tools. We implement VoxelPrompt with PyTorch [125] and use Python as the programming language of φ and Ω . To support the wide range of imaging operations required by \mathcal{T} , we develop and use a PyTorch library of volumetric medical image utilities, called *Voxel*, which we release as an open-source package at github.com/dalcalab/voxel.

Agent Model. We implement the agent model α as a decoder-only transformer stack, using a randomly initialized LLaMA architecture [126, 127] with 16 transformer layers, a hidden representation of size $d = 512$, a linear representation of size 2,048, and 32 attention heads. We use the pre-computed tokenizer released with LLaMA 2, which includes a vocabulary of size $\gamma = 32,000$.

To split η^ϕ and η^φ in practice, we first transform η embeddings into a sequence of max-probability tokens. We extract η^ϕ from all sequence positions that immediately follow special token <MOD>, and we extract η^φ from all remaining positions. The agent α predicts <MOD> and subsequent η^ϕ features after every volume encoding and generation function argument. We project η^ϕ embeddings

to ϕ using a fully-connected layer with 32 output channels and SiLU activation.

Volume Encoder and Generator Models. We implement m_{enc} and m_{gen} as the respective down-sampling and up-sampling arms of a six-level UNet-like model [128]. Each level consists of a 3D convolutional layer followed by a latent feature ϕ mixing layer and stream interaction layer with $b = 32$, both defined in Section 3.1. All layers use SiLU activations. The spatial outputs at every level are channel-normalized with a group size of four, then max-pooled (m_{enc}) or trilinearly upsampled (m_{gen}) by a factor of two. Convolution kernels have size 3^3 , with 32 output channels at the top resolution level and 96 output channels at all other levels.

For all input volume streams, we populate \mathcal{E} with spatial features output at each level in m_{enc} . We use these latent features as skip-connections to corresponding level inputs in the generator m_{gen} , which predicts volumes through a convolutional layer with one output channel. To generate segmentations, we use sigmoid activation. We process images in their original acquisition resolution and shape by implementing a novel, native-space convolutional operation (Appendix A.1).

Optimization. We train VoxelPrompt using the Adam optimizer [129] with an initial learning rate of 10^{-4} , a batch size of one, and 10 gradient accumulation steps on an NVIDIA A100 GPU. We halve the learning rate after 10^5 steps with no improvement in validation accuracy, stopping training after four sets of learning rate updates. We set the volume loss weight $\lambda = 0.1$.

4 Task and Data Design

We handcraft a dataset \mathcal{T} of brain imaging tasks that involve a wide range of image acquisitions, segmentation protocols, and annotation types. While broadly diverse, this task set is still preliminary and not meant to encompass the entire spectrum of possible objectives in brain image analysis. We design \mathcal{T} to encompass a set of heterogeneous tasks that evaluate the promise of VoxelPrompt’s joint generation of analytical instructions, spatial delineations, and natural language descriptions.

4.1 Tasks

We include in \mathcal{T} a set of clinically-orientated objectives, which are broadly categorized as either ROI processing or pathology description tasks. For each task, we provide ground-truth code φ^* , used in training and evaluation.

Quantitative ROI Processing. Quantitative processing tasks involve image feature segmentation, optionally followed by downstream steps to compute ROI measures.

We include a standard segmentation task for all structures and pathology classes in our dataset.

Downstream processing tasks use predicted segmentations, sometimes in conjunction with the input image volumes. For example, some tasks involve removing, extracting, or cropping the field of view (FOV) around a segmented region. Others use segmentations to compute ROI-specific statistics of the image signal intensities, including mean intensity or signal-to-noise ratio (SNR). Morphological tasks analyze ROI shape and involve the computation of total volume, bounding box dimensions, or the individual height, width, and depth of a segmented structure. We also include tasks that compute and compare such metrics across multiple segmentations. For example, longitudinal tasks measure change in ROI properties across a series of scan sessions, and multi-region tasks compare metrics from different ROIs in single session.

For each ROI processing task, ground-truth code φ^* includes a sequence of functions to (1) encode the input volumes, (2) read the encoded volume features, and (3) generate a segmentation map for each ROI relevant to the task. Depending on the task, further analysis may be required, and we include functions that (4) operate on these segmentations (and possibly the input volumes) to compute intermediate metrics. Lastly, we append functions that (5) read the values of resulting metrics and (6) format them into an output message. Figure 2 illustrates the instruction forward-pass for a task that measures longitudinal change in tumor size.

Open-Language Classification. Another set of tasks include the generation of language-based image characterizations. We formulate these tasks as classification-style question-answering problems, in which VoxelPrompt outputs natural language corresponding to a text response from a finite set of possible answers.

For example, one task involves classifying lesion image signal intensity as either hyperintense, hypointense, or isointense relative to surrounding healthy tissue. Another set of tasks involves identifying anatomical lesion location. Possible supratentorial locations include the frontal, parietal, occipital, temporal, insular lobes, the lateral ventricles, and the posterior (PCA), middle (MCA), and anterior (ACA) cerebral arterial vascular territories. Infratentorial lesion locations include the brainstem, cerebellum, fourth ventricle, and cerebellopontine angle. We also include tasks that require integrating information across multiple input images. For example, these involve detecting whether a lesion restricts diffusion, given both an DWI and ADC map, or whether a lesion signal enhances after intravenous contrast administration, given both pre- and post-contrast scans.

We handcraft a target language response for all possible answers to these classification-style tasks. For each task, we construct the ground-truth instruction code φ^* with functions to (1) encode the input volumes, (2) read

the encoded volume features, and (3) output a text response with the correct natural language answer.

4.2 Prompt Synthesis

We develop a combinatorial strategy to synthesize a diverse set of input prompts to train VoxelPrompt. For a task τ , we establish a set of prompt templates \mathcal{P}_τ , which serve as a basis for synthesizing text. They include placeholders to accommodate multiple words, terminologies, and phrases with similar meanings. We compile a list of interchangeable text \mathcal{C}_k for each placeholder k . To generate a prompt p for task τ during training, we randomly sample a template from \mathcal{P}_τ , then fill each placeholder k with text sampled from \mathcal{C}_k . This process is recursive, as a single placeholder may include other placeholders. The distribution of prompts encompasses a range of clinical and imaging terminologies, as well as linguistic variations across tenses, syntactic structures, and lexical choices.

4.3 Images

We assemble and annotate a collection of 6,925 3D brain MRI and CT scans from 15 public datasets, and we generate segmentations corresponding to 185 different bilateral anatomical targets and 14 pathology classes. The MRI collection includes images acquired with T1-weighted (T1w), T2-weighted (T2w), FLAIR, proton-density (PD), gradient echo (GRE), and diffusion-weighted (DWI) sequences, with various scan resolutions. The subjects are divided into training, validation, and test sets, with 4,852, 213, and 1,860 3D images, respectively.

Anatomical Segmentations. We generate segmentations for whole-brain anatomical structures on images from the FSM [10], OASIS [130, 131], Mind Brain Body [132], IBC [133], CERMEP [134], and Forrest Gump [135] cohorts, using established automated methods [4, 10, 136]. We select high-quality acquisitions and thoroughly inspect and correct errors in the label maps. Additionally, we make use of multiple image atlases with precomputed segmentations [137, 138], and we manually segment additional structures across a small group of 16 images. Appendix A.2 provides a complete list of anatomical labels.

Pathology Segmentations. We collect scans with pathology from the BraTS [30], ISLES [139], ATLAS [140], and WMH [28] datasets. These provide segmentations for glioma, edema, contrast-enhancing tissue, infarcts, and white matter hyperintensities (leukoaraiosis).

Additionally, we compile data from the *Radiopaedia* online resource (Appendix A.7), assembling images of conditions that include infarcts, arachnoid cysts, epidermoid cysts, cavum veli interpositi, glioma, choroid plexus papilloma, meningioma, central neurocytoma, and intracranial hemorrhages. We manually delineate the le-

sions and their various sub-components, including edema, enhancing tissue, and heterogeneous intralésion features.

During training, we apply a synthesis procedure to conditionally generate lesions with a variety of location and signal characteristics in healthy brain parenchyma. We detail this mechanism in Appendix A.3.

Pathology Characterization. We manually annotate properties of lesions, including anatomical location within the brain, image intensity properties, and relative position or size compared to other features present in the scan. When appropriate, we also mark whether a lesion restricts the diffusion of water or whether it enhances (increases in signal) after a contrast agent is administered to the subject.

Preprocessing. We normalize voxel intensities within the range $[0, 1]$, spatially conform the volume array to a right-anterior-superior (RAS) orientation, and crop images to a 20 mm margin around the cranial cavity. We co-register all images acquired from each subject [141]. In training, we augment images by applying random affine transformations, spatial intensity distortions, exponential scaling, lateral anatomical flipping, cropping, anatomical masking, and voxel resizing.

5 Experiments

We analyze the capability of VoxelPrompt to carry out both language-driven and computationally grounded image analysis across a range of tasks. We train VoxelPrompt on our handcrafted set of neuroimaging tasks, and we evaluate on a set of held-out imaging data. We first showcase a range of representative VoxelPrompt use cases through illustrative examples. Then, we quantitatively compare VoxelPrompt outputs with those of specialized model benchmarks for a subset of segmentation and language-based question-answering tasks. Our goal is to evaluate whether a single VoxelPrompt model can capture the individual accuracy of this collection of models, rather than attempt to surpass benchmark performance.

During evaluation, we use input prompts equivalent or similar to those synthesized for training. Unless otherwise stated, we pass all images for a given subject as input to VoxelPrompt and benchmark models.

5.1 Illustrative Use Cases

Multi-Task Capability. In Figure 1, we illustrate several results on held-out data that demonstrate the diversity of tasks VoxelPrompt can encompass. A single VoxelPrompt model can learn to localize a range of brain anatomy and pathology regions as well as mask or crop tissue groups for improved visual analysis. Within targeted ROIs, the model can extract statistical intensity metrics, such as average Hounsfield units or apparent diffusion coefficient

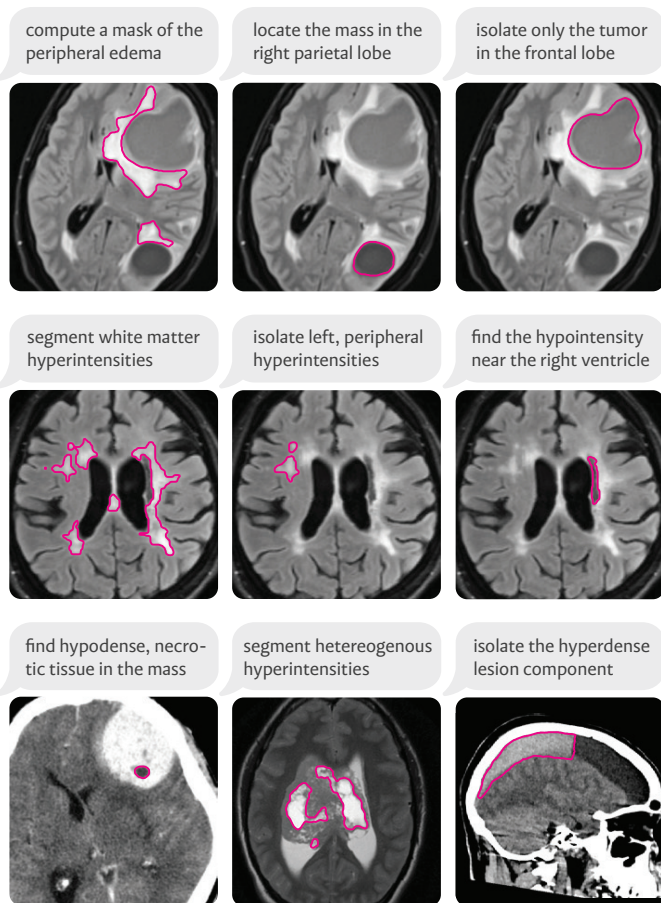


Figure 3. Natural language input prompts (shown above each image) enable targeted analysis of nuanced, context-specific image regions, especially for multi-lesion cases. Borders of segmentations predicted by VoxelPrompt are shown in purple.

(ADC) values, and derive measurements of structural morphology, such as total volume and extent dimensions.

VoxelPrompt can learn to compute and compare metrics across multiple ROIs, for instance, it can measure hippocampal asymmetry, normalize subcortical volumes by intracranial size, and quantify acute and chronic components of subdural hemorrhage. When provided with multiple scans, VoxelPrompt can measure longitudinal changes, such as tumor progression, ventricular growth in encephalitis, or signal decay in stroke progression. VoxelPrompt is able to characterize lesion locations and tissue properties, such as diffusion restriction (indicating areas of acute ischemia) and post-contrast enhancement (indicating blood-brain barrier disruption), by integrating information from multiple acquisitions simultaneously.

Flexible Analysis via Language. Figure 3 shows that VoxelPrompt supports flexible targeting of context-specific components in multifocal disease scenarios. Given language descriptors, the model can learn to isolate or differentiate lesions based on factors such as signal intensity,

size, relative position, or anatomical context (e.g., including hemisphere, arterial territory, or cerebral lobe).

5.2 Segmentation Accuracy

Image segmentation is a core component in learned ROI processing tasks. In this section, we compare the segmentation accuracy of VoxelPrompt with that of specialized models trained on specific labels as well as an existing state-of-the-art method. To generate segmentations, we explicitly prompt VoxelPrompt to “segment the ROI”, replacing “ROI” with the target region name or description. For bilateral brain structures, we prompt VoxelPrompt to segment the “left and right ROI”. We assess accuracy using the Dice coefficient [142] to measure overlap between ground-truth and predicted segmentations. When computing this overlap, we group bilateral structures together as a single label. We evaluate statistical differences in Dice between VoxelPrompt and each benchmark model through a paired *t*-test.

Specialized Benchmarks. To test if VoxelPrompt can match the combined performance of multiple specialized models, we optimize an individual, label-specific segmentation network for a subset of distinct ROIs in our dataset. This UNet-like benchmark architecture is equivalent to combining m_{enc} and m_{gen} , with each ϕ mixing layer replaced by a fully-connected layer (without ϕ inputs) to ensure comparable capacity to VoxelPrompt. We optimize each benchmark model with the soft Dice loss and we use all training images containing segmentations for a specific reference label. Since optimizing a specialized baseline for each ROI in our training dataset is computationally prohibitive, we select a subset of 10 anatomical and 7 pathology targets spanning diverse shapes and locations. In total, the resulting evaluation subset encompasses 638 held-out subjects, detailed in Appendix A.4.

State-of-the-Art Baseline. We also evaluate SynthSeg [8], a state-of-the-art method for multi-class brain segmentation that generalizes across the diverse acquisition contrasts exhibited in our image dataset. We use the more recent SynthSeg v2, which also parcellates the cortex into discrete subregions. For evaluation, we organize a structural MRI test set of 108 images, which contain ground-truth segmentations for 45 individual anatomical structures that are segmented by SynthSeg. Since SynthSeg supports only one input image in the forward pass, we evaluate segmentation performance individually, for each image in a scan session.

Results. Figure 4 (top) shows that VoxelPrompt matches ($p > 0.05$) or exceeds ($p < 0.05$) the performance of 13/17 single-task benchmarks. The mean Dice score difference (VoxelPrompt relative to benchmarks) is $+4.3 \pm 5.7\%$ across pathology targets and $-0.1 \pm 0.3\%$ across anatomical struc-

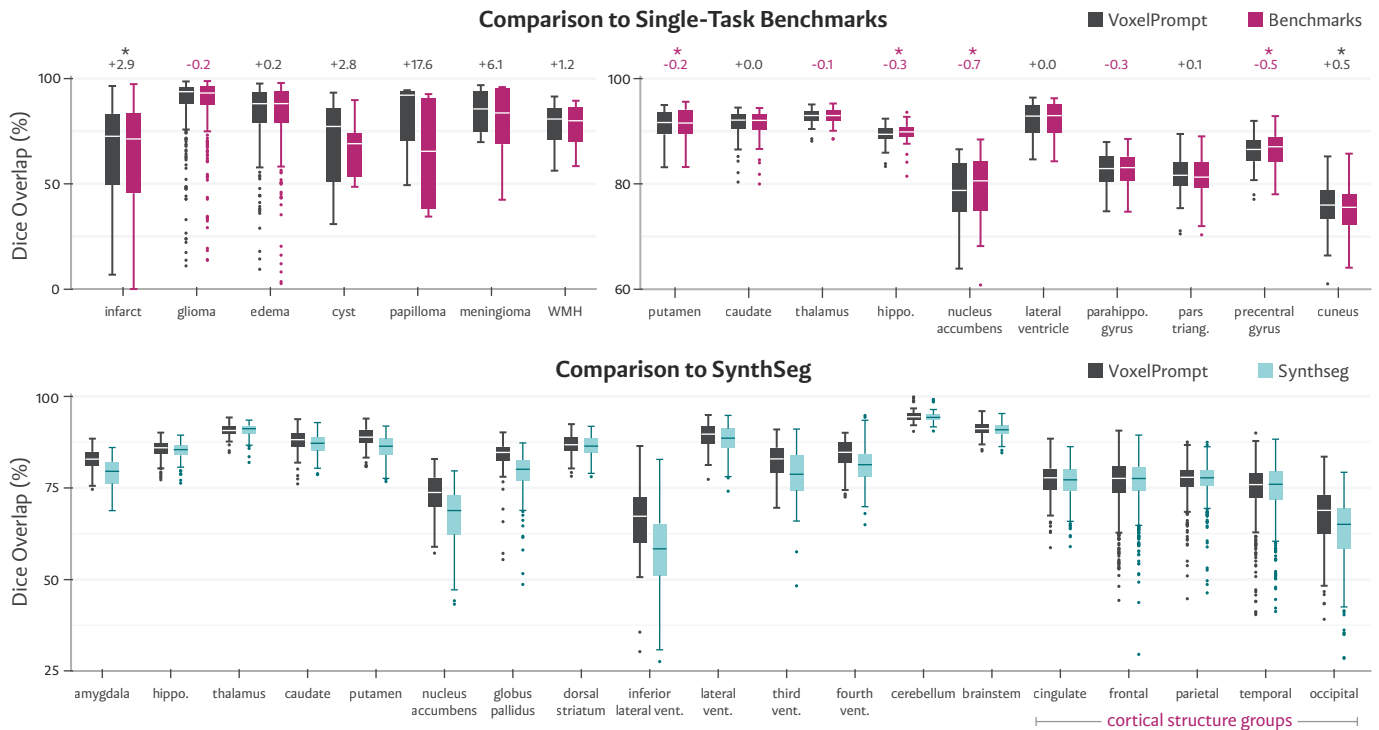


Figure 4. VoxelPrompt (black) yields segmentations with accuracy that matches or exceeds that of specialized single-task (purple) and state-of-the-art (blue) brain segmentation benchmarks. We plot the Dice score between estimated segmentations and the ground truth for a set of label targets, with the average differences between VoxelPrompt and the single-task benchmarks above each label plot. Significant differences ($p < 0.05$, paired t -test) are marked with an asterisk. For visual simplicity in the SynthSeg comparison, we group results for cortical regions by their associated cortical lobe.

tures. For the four ROIs in which VoxelPrompt significantly under-performs these benchmarks, the mean difference in Dice is only $-0.4 \pm 0.2\%$. Figure 4 (bottom) shows that VoxelPrompt significantly ($p < 0.05$) outperforms SynthSeg on 23/45 ROIs and exhibits a mean Dice improvement of $+1.1 \pm 2.3\%$ over all 45 structures. Overall, this demonstrates that a single VoxelPrompt model can perform on par with individual, specialized segmentation tools across a wide range of targets.

5.3 Pathology Characterization

We evaluate the ability of VoxelPrompt to characterize image features with predicted language description. Specifically, we focus on five pathology-based visual question-answering tasks (also used during training). These involve classifying lesion (1) signal intensity, (2) broad cerebral location, (3) stroke-affected vascular territory, (4) diffusion restriction, and (5) post-contrast enhancement.

For each of these tasks, we curate a subset of held-out subjects with relevant features while ensuring equal representation of possible classification categories in each subset. In total, the evaluation set consists of 102 cases, with per-task breakdowns detailed in Appendix A.5. During model evaluation, we consider a prediction as correct if the output natural language response exactly matches

the expected characterization. Using a paired t -test, we compare the VoxelPrompt per-task classification accuracy to that of multiple models, defined below.

Specialized Benchmarks. We compare VoxelPrompt to a set of classifier benchmarks, each trained for one of the five pathology characterization tasks in \mathcal{T} . As opposed to using language, the single-task benchmark models directly predict label probabilities for a fixed set of task-specific characterizations. We implement these models using the architecture of m_{enc} , with ϕ mixing layers replaced as in the benchmarks of the previous experiment. We reduce the spatial dimensions of the deepest encoder layer output using a global max operator, then we compute the max over all input volume streams. To compute classification probabilities for n possible descriptions, we pass the stream-pooled features to a fully-connected layer with n output channels and softmax activation. During benchmark optimization, we use the categorical cross-entropy loss on these predicted probabilities.

State-of-the-Art Baseline. We also compare VoxelPrompt to RadFM [77], the only publicly released, state-of-the-art architecture for medical visual question answering that can process multiple 3D images simultaneously. Overall, we find that the pretrained RadFM as well as universal 2D

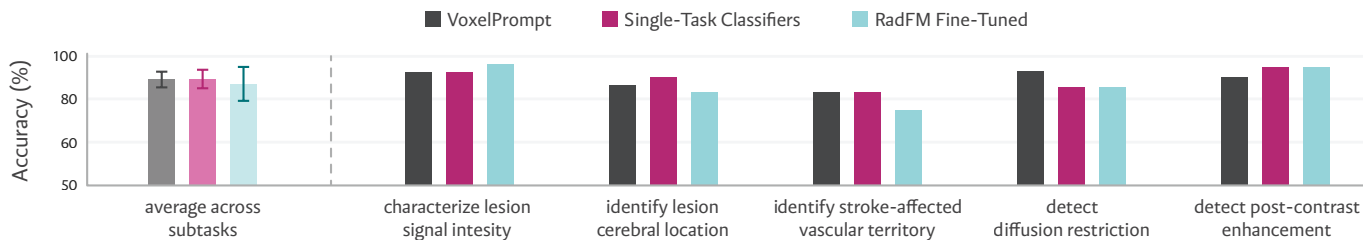


Figure 5. Accuracy of pathology characterization using natural language for five separate classification subtasks. Average subtask accuracy is shown on the left. VoxelPrompt (black) parallels the performance of individually-trained, single-task classifiers (purple) and a fine-tuned RadFM model (blue) – a state-of-the-art method for 3D visual question-answering.

vision-language models, such as ChatGPT [143], cannot generalize to the neuroimaging tasks used in this experiment (Appendix A.6). Therefore, we *fine-tune* RadFM on our subset of pathology characterization tasks, using training code released with the pretrained model weights. To fit the optimization within 80 GB of GPU memory, we keep only the first eight hidden transformer layers of the language model. We do not modify any other model components. As required by the vision transformer, we resize all input volume spatial dimensions to the nearest multiple of $32 \times 32 \times 4$. During fine-tuning, we use only the expected language response (without code) as target text.

Results. Figure 5 shows that VoxelPrompt achieves an average classification accuracy of $89.0 \pm 3.6\%$ over all tasks, matching the performance ($p > 0.05$) of the single-task benchmarks ($89.3 \pm 4.2\%$) as well as the fine-tuned RadFM model ($87.1 \pm 7.9\%$). These results demonstrate that VoxelPrompt can achieve language-based image characterization with comparable performance to specialized classification and medical vision-language architectures.

6 Discussion

We introduced VoxelPrompt, a vision-language agent that can perform diverse radiological tasks (Figure 1). This single, unified framework conducts medical image analyses that typically require a multitude of specialized models and extensive user oversight.

Grounded Analysis. To solve a desired task, the VoxelPrompt agent orchestrates the use of various computational tools, including instructable vision networks that can accurately segment hundreds of image features (Experiment 5.2). This approach provides results that are grounded by explicit image processing, leading to better reliability than existing vision-language models. For instance, rather than modelling metrics directly as estimated text, VoxelPrompt computes relevant outputs through a traceable sequence of operations, providing a level of transparency that is essential for clinical applications.

Flexible Language Prompting. In VoxelPrompt, natural

language prompting facilitates intuitive interaction and context-specific queries. Unlike interactive techniques relying on only bounding boxes, clicks, or in-context example pairs, language provides a compact mechanism to define detailed ROI targets with a vocabulary familiar to practitioners (Figure 3).

We achieve this flexibility through latent communication between the jointly-trained agent and vision networks, as opposed to selecting from a collection of specialized, pretrained segmentation models. Such an approach would face combinatorial challenges for context-specific analysis of ROIs distinguished by nuanced criteria, such as relative position or signal intensity. We demonstrate that VoxelPrompt matches the performance of individual segmentation benchmarks while enabling a flexible interaction mechanism for a landscape of goals.

Data Limitations. VoxelPrompt demonstrates the ability to effectively tackle a diverse set of ROI processing and language-based image characterization tasks. However, since we optimize the model from scratch, its utility is restricted to the scenarios covered by the training domain.

To extend the scope of VoxelPrompt, we plan to construct a comprehensive training dataset that spans a substantially larger range of imaging tasks and anatomical fields. We can incorporate real hospital data, along with associated text reports, to improve the ability of VoxelPrompt to generate key clinical documentation and align learned representations with complex pathologies seen in practice. Additionally, leveraging pretrained language models with broad medical, programming, and problem solving knowledge could establish a robust backbone to support generalization to unfamiliar tasks.

System Integration. As a code-predicting agent framework, VoxelPrompt can integrate with an array of external systems and APIs. This includes accessing medical databases to integrate patient records for additional context, pulling population-level statistics to support referential analysis, or implementing on-the-scanner interaction for real-time acquisition guidance. As an integrated interface, VoxelPrompt can grow to assist practitioners in efficiently navigating and interpreting imaging studies.

By combining natural language interaction, instructable vision models, and agent-based planning, we believe VoxelPrompt provides an advanced, multi-task system that promises to support the spectrum of real-world clinical and research imaging aims.

Acknowledgements

This work is supported in part by the National Institute of Biomedical Imaging and Bioengineering (R01 EB033773, T32 EB001680), the Harvard-MIT Neuroimaging Training Program, the National Science Foundation Graduate Research Fellowships Program, and Quanta Computer Inc.

References

- [1] John Ashburner and Karl J Friston. Unified segmentation. *neuroimage*, 26(3):839–851, 2005.
- [2] Robert W Cox. Afni: Software for analysis and visualization of functional magnetic resonance neuroimages. *Computers and Biomedical research*, 29(3):162–173, 1996.
- [3] Cameron Craddock, Sharad Sikka, Brian Cheung, Ranjeet Khanuja, Satrajit S Ghosh, Chaogan Yan, Qingyang Li, Daniel Lurie, Joshua Vogelstein, Randal Burns, et al. Towards automated analysis of connectomes: The configurable pipeline for the analysis of connectomes (c-pac). *Front Neuroinform*, 42(10.3389), 2013.
- [4] Bruce Fischl. Freesurfer. *Neuroimage*, 62(2):774–781, 2012.
- [5] Mark Jenkinson, Christian F Beckmann, Timothy EJ Behrens, Mark W Woolrich, and Stephen M Smith. Fsl. *Neuroimage*, 62(2):782–790, 2012.
- [6] David W Shattuck and Richard M Leahy. Brainsuite: An automated cortical surface identification tool. *Medical image analysis*, 6(2):129–142, 2002.
- [7] J-Donald Tournier, Robert Smith, David Raffelt, Rami Tabbara, Thijs Dhollander, Maximilian Pietsch, Daan Christiaens, Ben Jeurissen, Chun-Hung Yeh, and Alan Connelly. Mrtrix3: A fast, flexible and open software framework for medical image processing and visualisation. *Neuroimage*, 202:116137, 2019.
- [8] Benjamin Billot, Douglas N Greve, Oula Puonti, Axel Thielscher, Koen Van Leemput, Bruce Fischl, Adrian V Dalca, Juan Eugenio Iglesias, et al. Synthseg: Segmentation of brain mri scans of any contrast and resolution without retraining. *Medical image analysis*, 86:102789, 2023.
- [9] Jennifer Faber, David Kügler, Emad Bahrami, Lea-Sophie Heinz, Dagmar Timmann, Thomas M Ernst, Katerina Deike-Hofmann, Thomas Klockgether, Bart van de Warrenburg, Judith van Gaalen, et al. Cerebnet: A fast and reliable deep-learning pipeline for detailed cerebellum sub-segmentation. *Neuroimage*, 264:119703, 2022.
- [10] Douglas N Greve, Benjamin Billot, Devani Cordero, Andrew Hoopes, Malte Hoffmann, Adrian V Dalca, Bruce Fischl, Juan Eugenio Iglesias, and Jean C Augustinack. A deep learning toolbox for automatic segmentation of sub-cortical limbic structures from mri images. *Neuroimage*, 244:118610, 2021.
- [11] Leonie Henschel, Sailesh Conjeti, Santiago Estrada, Kersten Diers, Bruce Fischl, and Martin Reuter. Fastsurfer - a fast and accurate deep learning based neuroimaging pipeline. *NeuroImage*, 219:117012, 2020.
- [12] Manhua Liu, Fan Li, Hao Yan, Kundong Wang, Yixin Ma, Li Shen, Mingqing Xu, Alzheimer’s Disease Neuroimaging Initiative, et al. A multi-model deep convolutional neural network for automatic hippocampus segmentation and classification in alzheimer’s disease. *Neuroimage*, 208:116459, 2020.
- [13] Henry FJ Tregidgo, Sonja Soskic, Mark D Olchanyi, Juri Althonayan, Benjamin Billot, Chiara Maffei, Polina Golland, Anastasia Yendiki, Daniel C Alexander, Martina Bocchetta, et al. Domain-agnostic segmentation of thalamic nuclei from joint structural and diffusion mri. In *International Conference on Medical Image Computing and Computer-Assisted Intervention*, pages 247–257. Springer, 2023.
- [14] Adam Hilbert, Vince I Madai, Ela M Akay, Orhun U Aydin, Jonas Behland, Jan Sobesky, Ivana Galinovic, Ahmed A Khalil, Abdel A Taha, Jens Wuerfel, et al. Brave-net: fully automated arterial brain vessel segmentation in patients with cerebrovascular disease. *Frontiers in artificial intelligence*, 3:552258, 2020.
- [15] Michelle Livne, Jana Rieger, Orhun Utku Aydin, Abdel Aziz Taha, Ela Marie Akay, Tabea Kossen, Jan Sobesky, John D Kelleher, Kristian Hildebrand, Dietmar Frey, et al. A u-net deep learning framework for high performance vessel segmentation in patients with cerebrovascular disease. *Frontiers in neuroscience*, 13:97, 2019.
- [16] Qi Lu, Wan Liu, Zhizheng Zhuo, Yuxing Li, Yunyun Duan, Pinnan Yu, Liying Qu, Chuyang Ye, and Yaou Liu. A transfer learning approach to few-shot segmentation of novel white matter tracts. *Medical Image Analysis*, 79:102454, 2022.
- [17] Jakob Wasserthal, Peter Neher, and Klaus H Maier-Hein. Tractseg-fast and accurate white matter tract segmentation. *NeuroImage*, 183:239–253, 2018.
- [18] Fan Zhang, Suheyly Cetin Karayumak, Nico Hoffmann, Yogesh Rathi, Alexandra J Golby, and Lauren J O’Donnell. Deep white matter analysis (deepwma): fast and consistent tractography segmentation. *Medical Image Analysis*, 65:101761, 2020.
- [19] Bjoern H Menze, Andras Jakab, Stefan Bauer, Jayashree Kalpathy-Cramer, Keyvan Farahani, Justin Kirby, Yuliya Burren, Nicole Porz, Johannes Slotboom, Roland Wiest, et al. The multimodal brain tumor image segmentation benchmark (brats). *IEEE transactions on medical imaging*, 34(10):1993–2024, 2014.

- [20] Ramin Ranjbarzadeh, Abbas Bagherian Kasgari, Saeid Jafarzadeh Ghoushchi, Shokofeh Anari, Maryam Naseri, and Malika Bendeche. Brain tumor segmentation based on deep learning and an attention mechanism using mri multi-modalities brain images. *Scientific Reports*, 11(1):1–17, 2021.
- [21] Wenxuan Wang, Chen Chen, Meng Ding, Jianguyun Li, Hong Yu, and Sen Zha. Transbts: Multimodal brain tumor segmentation using transformer. *ArXiv*, abs/2103.04430, 2021.
- [22] Yao Zhang, Nanjun He, Jiawei Yang, Yuexiang Li, Dong Wei, Yawen Huang, Yang Zhang, Zhiqiang He, and Yefeng Zheng. mmformer: Multimodal medical transformer for incomplete multimodal learning of brain tumor segmentation. *ArXiv*, abs/2206.02425, 2022.
- [23] Murtadha D Hssayeni, Muayad S Croock, Aymen D Salman, Hassan Falah Al-Khafaji, Zakaria A Yahya, and Behnaz Ghoraani. Intracranial hemorrhage segmentation using a deep convolutional model. *Data*, 5(1):14, 2020.
- [24] Liang Chen, Paul Bentley, and Daniel Rueckert. Fully automatic acute ischemic lesion segmentation in dwi using convolutional neural networks. *NeuroImage : Clinical*, 15: 633 – 643, 2017.
- [25] Chin-Fu Liu, Johnny T. C. Hsu, Xin Xu, Sandhya Ramachandran, Victor Wang, Michael I. Miller, Argye Elizabeth Hillis, Andreia Vasconcellos Faria, Max Steven J. Gregory W. Stephen M. James C. Werner Do Wintermark Warach Albers Davis Grotta Hacke Kang K, Max Wintermark, Steven J. Warach, Gregory W. Albers, Stephen M. Davis, James Charles Grotta, Werner Hacke, Dong-Wha Kang, Chelsea Kidwell, Walter J. Koroshetz, Kennedy R. Lees, Michael H. Lev, David S. Liebeskind, A. Gregory Sorensen, Vincent N. Thijs, Götz Thomalla, Joanna Marguerite Wardlaw, and Marie Luby. Deep learning-based detection and segmentation of diffusion abnormalities in acute ischemic stroke. *Communications Medicine*, 1, 2021.
- [26] Sanaz Nazari-Farsani, Yannan Yu, Rui Duarte Armindo, Maarten G. Lansberg, David S. Liebeskind, Gregory W. Albers, Søren Christensen, Craig S. Levin, and Greg Zaharchuk. Predicting final ischemic stroke lesions from initial diffusion-weighted images using a deep neural network. *NeuroImage : Clinical*, 37, 2022.
- [27] Ricardo Guerrero, Chen Qin, Ozan Oktay, Christopher Bowles, Liang Chen, Richard Joules, Robin Wolz, M del C Valdés-Hernández, David Alexander Dickie, Joanna Wardlaw, et al. White matter hyperintensity and stroke lesion segmentation and differentiation using convolutional neural networks. *NeuroImage: Clinical*, 17:918–934, 2018.
- [28] Hugo J Kuijff, J Matthijs Biesbroek, Jeroen De Bresser, Rutger Heinen, Simon Andermatt, Mariana Bento, Matt Berseth, Mikhail Belyaev, M Jorge Cardoso, Adria Casamitjana, et al. Standardized assessment of automatic segmentation of white matter hyperintensities and results of the wmh segmentation challenge. *IEEE transactions on medical imaging*, 38(11):2556–2568, 2019.
- [29] Walter HL Pinaya, Petru-Daniel Tudosiu, Robert Gray, Geraint Rees, Parashkev Nachev, Sebastien Ourselin, and M Jorge Cardoso. Unsupervised brain imaging 3d anomaly detection and segmentation with transformers. *Medical Image Analysis*, 79:102475, 2022.
- [30] Ujjwal Baid, Satyam Ghodasara, Suyash Mohan, Michel Bilello, Evan Calabrese, Errol Colak, Keyvan Farahani, Jayashree Kalpathy-Cramer, Felipe C Kitamura, Sarthak Pati, et al. The rsna-asnr-miccai brats 2021 benchmark on brain tumor segmentation and radiogenomic classification. *arXiv preprint arXiv:2107.02314*, 2021.
- [31] Soumick Chatterjee, Faraz Ahmed Nizamani, Andreas Nürnberger, and Oliver Speck. Classification of brain tumours in mr images using deep spatiotemporal models. *Scientific Reports*, 12(1):1505, 2022.
- [32] James H Cole, Rudra PK Poudel, Dimosthenis Tsagkraloulis, Matthan WA Caan, Claire Steves, Tim D Spector, and Giovanni Montana. Predicting brain age with deep learning from raw imaging data results in a reliable and heritable biomarker. *NeuroImage*, 163:115–124, 2017.
- [33] Jeyeon Lee, Brian J Burkett, Hoon-Ki Min, Matthew L Senjem, Emily S Lundt, Hugo Botha, Jonathan Graff-Radford, Leland R Barnard, Jeffrey L Gunter, Christopher G Schwarz, et al. Deep learning-based brain age prediction in normal aging and dementia. *Nature Aging*, 2(5):412–424, 2022.
- [34] Han Peng, Weikang Gong, Christian F Beckmann, Andrea Vedaldi, and Stephen M Smith. Accurate brain age prediction with lightweight deep neural networks. *Medical image analysis*, 68:101871, 2021.
- [35] Silvia Basaia, Federica Agosta, Luca Wagner, Elisa Canu, Giuseppe Magnani, Roberto Santangelo, Massimo Filippi, Alzheimer’s Disease Neuroimaging Initiative, et al. Automated classification of alzheimer’s disease and mild cognitive impairment using a single mri and deep neural networks. *NeuroImage: Clinical*, 21:101645, 2019.
- [36] Junhao Wen, Elina Thibeau-Sutre, Mauricio Diaz-Melo, Jorge Samper-González, Alexandre Routier, Simona Botani, Didier Dormont, Stanley Durrleman, Ninon Burgos, Olivier Colliot, et al. Convolutional neural networks for classification of alzheimer’s disease: Overview and reproducible evaluation. *Medical image analysis*, 63:101694, 2020.
- [37] Hongming Li, Mohamad Habes, David A Wolk, Yong Fan, Alzheimer’s Disease Neuroimaging Initiative, et al. A deep learning model for early prediction of alzheimer’s disease dementia based on hippocampal magnetic resonance imaging data. *Alzheimer’s & Dementia*, 15(8):1059–1070, 2019.
- [38] Garam Lee, Kwangsik Nho, Byungkon Kang, Kyung-Ah Sohn, and Dokyoon Kim. Predicting alzheimer’s disease progression using multi-modal deep learning approach. *Scientific reports*, 9(1):1952, 2019.
- [39] Rich Caruana. Multitask learning. *Machine learning*, 28(1): 41–75, 1997.

- [40] Ozan Sener and Vladlen Koltun. Multi-task learning as multi-objective optimization. *Advances in neural information processing systems*, 31, 2018.
- [41] Yan Zhao, Xiuying Wang, Tongtong Che, Guoqing Bao, and Shuyu Li. Multi-task deep learning for medical image computing and analysis: A review. *Computers in Biology and Medicine*, 153:106496, 2023.
- [42] Amine Amyar, Romain Modzelewski, Hua Li, and Su Ruan. Multi-task deep learning based ct imaging analysis for covid-19 pneumonia: Classification and segmentation. *Computers in biology and medicine*, 126:104037, 2020.
- [43] Mohamed S Elmahdy, Laurens Beljaards, Sahar Yousefi, Hessam Sokooti, Fons Verbeek, Uulke A Van Der Heide, and Marius Staring. Joint registration and segmentation via multi-task learning for adaptive radiotherapy of prostate cancer. *IEEE Access*, 9:95551–95568, 2021.
- [44] Simon Graham, Quoc Dang Vu, Mostafa Jahanifar, Shan E Ahmed Raza, Fayyaz Minhas, David Snead, and Nasir Rajpoot. One model is all you need: multi-task learning enables simultaneous histology image segmentation and classification. *Medical Image Analysis*, 83:102685, 2023.
- [45] Bo Li, Wiro J Niessen, Stefan Klein, Marius de Groot, M Arfan Ikram, Meike W Vernooij, and Esther E Bron. A hybrid deep learning framework for integrated segmentation and registration: evaluation on longitudinal white matter tract changes. In *Medical Image Computing and Computer Assisted Intervention—MICCAI 2019: 22nd International Conference, Shenzhen, China, October 13–17, 2019, Proceedings, Part III* 22, pages 645–653. Springer, 2019.
- [46] David Tellez, Diederik Höppener, Cornelis Verhoef, Dirk Grünhagen, Pieter Nierop, Michal Drozdal, Jeroen Laak, and Francesco Ciompi. Extending unsupervised neural image compression with supervised multitask learning. In *Medical Imaging with Deep Learning*, pages 770–783. PMLR, 2020.
- [47] Junlong Cheng, Jin Ye, Zhongying Deng, Jianpin Chen, Tianbin Li, Haoyu Wang, Yanzhou Su, Ziyang Huang, Jilong Chen, Lei Jiang, et al. Sam-med2d. *arXiv preprint arXiv:2308.16184*, 2023.
- [48] Xiangde Luo, Guotai Wang, Tao Song, Jingyang Zhang, Michael Aertsen, Jan Deprest, Sebastien Ourselin, Tom Vercauteren, and Shaoting Zhang. Mideepseg: Minimally interactive segmentation of unseen objects from medical images using deep learning. *Medical image analysis*, 72:102102, 2021.
- [49] Jun Ma, Yuting He, Feifei Li, Lin Han, Chenyu You, and Bo Wang. Segment anything in medical images. *Nature Communications*, 15(1):654, 2024.
- [50] Tomas Sakinis, Fausto Milletari, Holger Roth, Panagiotis Korfiatis, Petro Kostandy, Kenneth Philbrick, Zeynetin Akkus, Ziyue Xu, Daguang Xu, and Bradley J Erickson. Interactive segmentation of medical images through fully convolutional neural networks. *arXiv preprint arXiv:1903.08205*, 2019.
- [51] Hallee E Wong, Marianne Rakic, John Guttag, and Adrian V Dalca. Scribbleprompt: Fast and flexible interactive segmentation for any medical image. *arXiv preprint arXiv:2312.07381*, 2023.
- [52] Sewon Min, Mike Lewis, Luke Zettlemoyer, and Hanneh Hajishirzi. Metaicl: Learning to learn in context. *arXiv preprint arXiv:2110.15943*, 2021.
- [53] Sang Michael Xie, Aditi Raghunathan, Percy Liang, and Tengyu Ma. An explanation of in-context learning as implicit bayesian inference. *arXiv preprint arXiv:2111.02080*, 2021.
- [54] Victor Ion Butoi, Jose Javier Gonzalez Ortiz, Tianyu Ma, Mert R Sabuncu, John Guttag, and Adrian V Dalca. Universeg: Universal medical image segmentation. *arXiv preprint arXiv:2304.06131*, 2023.
- [55] Cheng Ouyang, Carlo Biffi, Chen Chen, Turkay Kart, Huaqi Qiu, and Daniel Rueckert. Self-supervised learning for few-shot medical image segmentation. *IEEE Transactions on Medical Imaging*, 41(7):1837–1848, 2022.
- [56] Marianne Rakic, Hallee E Wong, Jose Javier Gonzalez Ortiz, Beth Cimini, John Guttag, and Adrian V Dalca. Tyche: Stochastic in-context learning for medical image segmentation. *arXiv preprint arXiv:2401.13650*, 2024.
- [57] Abhijit Guha Roy, Shayan Siddiqui, Sebastian Pölsterl, Nassir Navab, and Christian Wachinger. ‘squeeze & excite’guided few-shot segmentation of volumetric images. *Medical image analysis*, 59:101587, 2020.
- [58] Steffen Czolbe and Adrian V Dalca. Neuralizer: General neuroimage analysis without re-training. In *Proceedings of the IEEE/CVF Conference on Computer Vision and Pattern Recognition*, pages 6217–6230, 2023.
- [59] Alec Radford, Jong Wook Kim, Chris Hallacy, Aditya Ramesh, Gabriel Goh, Sandhini Agarwal, Girish Sastry, Amanda Askell, Pamela Mishkin, Jack Clark, et al. Learning transferable visual models from natural language supervision. In *International conference on machine learning*, pages 8748–8763. PMLR, 2021.
- [60] Alistair EW Johnson, Tom J Pollard, Seth J Berkowitz, Nathaniel R Greenbaum, Matthew P Lungren, Chih-ying Deng, Roger G Mark, and Steven Horng. Mimic-cxr, a de-identified publicly available database of chest radiographs with free-text reports. *Scientific data*, 6(1):317, 2019.
- [61] Weixiong Lin, Ziheng Zhao, Xiaoman Zhang, Chaoyi Wu, Ya Zhang, Yanfeng Wang, and Weidi Xie. Pmc-clip: Contrastive language-image pre-training using biomedical documents. In *International Conference on Medical Image Computing and Computer-Assisted Intervention*, pages 525–536. Springer, 2023.
- [62] Obioma Pelka, Sven Koitka, Johannes Rückert, Felix Nensa, and Christoph M Friedrich. Radiology objects in context (roco): a multimodal image dataset. In *Intravascular Imaging and Computer Assisted Stenting and Large-Scale Annotation of Biomedical Data and Expert Label Synthesis: 7th*

Joint International Workshop, CVII-STENT 2018 and Third International Workshop, LABELS 2018, Held in Conjunction with MICCAI 2018, Granada, Spain, September 16, 2018, Proceedings 3, pages 180–189. Springer, 2018.

- [63] Sheng Zhang, Yanbo Xu, Naoto Usuyama, Hanwen Xu, Jaspreet Bagga, Robert Tinn, Sam Preston, Rajesh Rao, Mu Wei, Naveen Valluri, et al. Biomedclip: a multi-modal biomedical foundation model pretrained from fifteen million scientific image-text pairs. *arXiv preprint arXiv:2303.00915*, 2023.
- [64] Qihui Chen, Xinyue Hu, Zirui Wang, and Yi Hong. Med-clip: Bootstrapping language-image pre-training from 3d medical images and texts. *arXiv preprint arXiv:2305.10799*, 2023.
- [65] Yinda Chen, Che Liu, Wei Huang, Sibao Cheng, Rossella Arcucci, and Zhiwei Xiong. Generative text-guided 3d vision-language pretraining for unified medical image segmentation. *arXiv preprint arXiv:2306.04811*, 2023.
- [66] Zhihong Chen, Guanbin Li, and Xiang Wan. Align, reason and learn: Enhancing medical vision-and-language pre-training with knowledge. In *Proceedings of the 30th ACM International Conference on Multimedia*, pages 5152–5161, 2022.
- [67] Sedigheh Eslami, Christoph Meinel, and Gerard De Melo. Pubmedclip: How much does clip benefit visual question answering in the medical domain? In *Findings of the Association for Computational Linguistics: EACL 2023*, pages 1181–1193, 2023.
- [68] Yash Khare, Viraj Bagal, Minesh Mathew, Adithi Devi, U Deva Priyakumar, and CV Jawahar. Mmbert: Multi-modal bert pretraining for improved medical vqa. In *2021 IEEE 18th International Symposium on Biomedical Imaging (ISBI)*, pages 1033–1036. IEEE, 2021.
- [69] Chunyuan Li, Cliff Wong, Sheng Zhang, Naoto Usuyama, Haotian Liu, Jianwei Yang, Tristan Naumann, Hoifung Poon, and Jianfeng Gao. Llava-med: Training a large language-and-vision assistant for biomedicine in one day. *Advances in Neural Information Processing Systems*, 36, 2024.
- [70] Bo Liu, Li-Ming Zhan, Li Xu, and Xiao-Ming Wu. Medical visual question answering via conditional reasoning and contrastive learning. *IEEE transactions on medical imaging*, 42(5):1532–1545, 2022.
- [71] Jong Hak Moon, Hyungyung Lee, Woncheol Shin, Young-Hak Kim, and Edward Choi. Multi-modal understanding and generation for medical images and text via vision-language pre-training. *IEEE Journal of Biomedical and Health Informatics*, 26(12):6070–6080, 2022.
- [72] Michael Moor, Qian Huang, Shirley Wu, Michihiro Yasunaga, Yash Dalmia, Jure Leskovec, Cyril Zakka, Eduardo Pontes Reis, and Pranav Rajpurkar. Med-flamingo: a multimodal medical few-shot learner. In *Machine Learning for Health (ML4H)*, pages 353–367. PMLR, 2023.
- [73] Philip Müller, Georgios Kaissis, Congyu Zou, and Daniel Rueckert. Joint learning of localized representations from medical images and reports. In *European Conference on Computer Vision*, pages 685–701. Springer, 2022.
- [74] Xiaosong Wang, Ziyue Xu, Leo Tam, Dong Yang, and Daguang Xu. Self-supervised image-text pre-training with mixed data in chest x-rays. *arXiv preprint arXiv:2103.16022*, 2021.
- [75] Zifeng Wang, Zhenbang Wu, Dinesh Agarwal, and Jimeng Sun. Medclip: Contrastive learning from unpaired medical images and text. *arXiv preprint arXiv:2210.10163*, 2022.
- [76] Chaoyi Wu, Xiaoman Zhang, Ya Zhang, Yanfeng Wang, and Weidi Xie. Medklip: Medical knowledge enhanced language-image pre-training in radiology. *arXiv preprint arXiv:2301.02228*, 2023.
- [77] Chaoyi Wu, Xiaoman Zhang, Ya Zhang, Yanfeng Wang, and Weidi Xie. Towards generalist foundation model for radiology. *arXiv preprint arXiv:2308.02463*, 2023.
- [78] Yuhao Zhang, Hang Jiang, Yasuhide Miura, Christopher D Manning, and Curtis P Langlotz. Contrastive learning of medical visual representations from paired images and text. In *Machine Learning for Healthcare Conference*, pages 2–25. PMLR, 2022.
- [79] Xiaoman Zhang, Chaoyi Wu, Ziheng Zhao, Weixiong Lin, Ya Zhang, Yanfeng Wang, and Weidi Xie. Pmc-vqa: Visual instruction tuning for medical visual question answering. *arXiv preprint arXiv:2305.10415*, 2023.
- [80] Shruthi Bannur, Kenza Bouzid, Daniel C Castro, Anton Schwaighofer, Sam Bond-Taylor, Maximilian Ilse, Fernando Pérez-García, Valentina Salvatelli, Harshita Sharma, Felix Meissen, et al. Maira-2: Grounded radiology report generation. *arXiv preprint arXiv:2406.04449*, 2024.
- [81] Zhongzhen Huang, Xiaofan Zhang, and Shaoting Zhang. Kiut: Knowledge-injected u-transformer for radiology report generation. In *Proceedings of the IEEE/CVF Conference on Computer Vision and Pattern Recognition*, pages 19809–19818, 2023.
- [82] Stephanie L Hyland, Shruthi Bannur, Kenza Bouzid, Daniel C Castro, Mercy Ranjit, Anton Schwaighofer, Fernando Pérez-García, Valentina Salvatelli, Shaury Srivastav, Anja Thieme, et al. Maira-1: A specialised large multimodal model for radiology report generation. *arXiv preprint arXiv:2311.13668*, 2023.
- [83] Jiayu Lei, Xiaoman Zhang, Chaoyi Wu, Lisong Dai, Ya Zhang, Yanyong Zhang, Yanfeng Wang, Weidi Xie, and Yuehua Li. Autorg-brain: Grounded report generation for brain mri. *arXiv preprint arXiv:2407.16684*, 2024.
- [84] Mingjie Li, Bingqian Lin, Zicong Chen, Haokun Lin, Xiaodan Liang, and Xiaojun Chang. Dynamic graph enhanced contrastive learning for chest x-ray report generation. In *Proceedings of the IEEE/CVF Conference on Computer Vision and Pattern Recognition*, pages 3334–3343, 2023.

- [85] Guanxiong Liu, Tzu-Ming Harry Hsu, Matthew McDermott, Willie Boag, Wei-Hung Weng, Peter Szolovits, and Marzyeh Ghassemi. Clinically accurate chest x-ray report generation. In *Machine Learning for Healthcare Conference*, pages 249–269. PMLR, 2019.
- [86] Mashood Mohammad Mohsan, Muhammad Usman Akram, Ghulam Rasool, Norah Saleh Alghamdi, Muhammad Abdullah Aamer Baqai, and Muhammad Abbas. Vision transformer and language model based radiology report generation. *IEEE Access*, 11:1814–1824, 2022.
- [87] Chantal Pellegrini, Ege Özsoy, Benjamin Busam, Nassir Navab, and Matthias Keicher. Radialog: A large vision-language model for radiology report generation and conversational assistance. *arXiv preprint arXiv:2311.18681*, 2023.
- [88] Jun Wang, Abhir Bhalerao, and Yulan He. Cross-modal prototype driven network for radiology report generation. In *European Conference on Computer Vision*, pages 563–579. Springer, 2022.
- [89] Zhanyu Wang, Lingqiao Liu, Lei Wang, and Luping Zhou. R2gengpt: Radiology report generation with frozen llms. *Meta-Radiology*, 1(3):100033, 2023.
- [90] Zhanyu Wang, Lingqiao Liu, Lei Wang, and Luping Zhou. Metransformer: Radiology report generation by transformer with multiple learnable expert tokens. In *Proceedings of the IEEE/CVF Conference on Computer Vision and Pattern Recognition*, pages 11558–11567, 2023.
- [91] Che Liu, Cheng Ouyang, Yinda Chen, Cesar César Quilodrán-Casas, Lei Ma, Jie Fu, Yike Guo, Anand Shah, Wenjia Bai, and Rossella Arcucci. T3d: Towards 3d medical image understanding through vision-language pre-training. *arXiv preprint arXiv:2312.01529*, 2023.
- [92] Hong-Yu Zhou, Subathra Adithan, Julián Nicolás Acosta, Eric J Topol, and Pranav Rajpurkar. A generalist learner for multifaceted medical image interpretation. *arXiv preprint arXiv:2405.07988*, 2024.
- [93] Zihan Li, Yunxiang Li, Qingde Li, Puyang Wang, Dazhou Guo, Le Lu, Dakai Jin, You Zhang, and Qingqi Hong. Lvit: language meets vision transformer in medical image segmentation. *IEEE transactions on medical imaging*, 2023.
- [94] Ziheng Zhao, Yao Zhang, Chaoyi Wu, Xiaoman Zhang, Ya Zhang, Yanfeng Wang, and Weidi Xie. One model to rule them all: Towards universal segmentation for medical images with text prompts. *arXiv preprint arXiv:2312.17183*, 2023.
- [95] Theodore Zhao, Yu Gu, Jianwei Yang, Naoto Usuyama, Ho Hin Lee, Tristan Naumann, Jianfeng Gao, Angela Crabtree, Brian Piening, Carlo Bifulco, et al. Biomed-parse: a biomedical foundation model for image parsing of everything everywhere all at once. *arXiv preprint arXiv:2405.12971*, 2024.
- [96] Christian Bluethgen, Pierre Chambon, Jean-Benoit Delbrouck, Rogier van der Sluijs, Małgorzata Połacin, Juan Manuel Zambrano Chaves, Tanishq Mathew Abraham, Shivanshu Purohit, Curtis P Langlotz, and Akshay S Chaudhari. A vision-language foundation model for the generation of realistic chest x-ray images. *Nature Biomedical Engineering*, pages 1–13, 2024.
- [97] Pierre Chambon, Christian Bluethgen, Jean-Benoit Delbrouck, Rogier Van der Sluijs, Małgorzata Połacin, Juan Manuel Zambrano Chaves, Tanishq Mathew Abraham, Shivanshu Purohit, Curtis P Langlotz, and Akshay Chaudhari. Roentgen: vision-language foundation model for chest x-ray generation. *arXiv preprint arXiv:2211.12737*, 2022.
- [98] Kyuri Kim, Yoonho Na, Sung-Joon Ye, Jimin Lee, Sung Soo Ahn, Ji Eun Park, and Hwiyoung Kim. Controllable text-to-image synthesis for multi-modality mr images. In *Proceedings of the IEEE/CVF Winter Conference on Applications of Computer Vision*, pages 7936–7945, 2024.
- [99] Riddhish Bhalodia, Ali Hatamizadeh, Leo Tam, Ziyue Xu, Xiaosong Wang, Evrim Turkbey, and Daguang Xu. Improving pneumonia localization via cross-attention on medical images and reports. In *Medical Image Computing and Computer Assisted Intervention—MICCAI 2021: 24th International Conference, Strasbourg, France, September 27–October 1, 2021, Proceedings, Part II 24*, pages 571–581. Springer, 2021.
- [100] Mark Chen, Jerry Tworek, Heewoo Jun, Qiming Yuan, Henrique Ponde De Oliveira Pinto, Jared Kaplan, Harri Edwards, Yuri Burda, Nicholas Joseph, Greg Brockman, et al. Evaluating large language models trained on code. *arXiv preprint arXiv:2107.03374*, 2021.
- [101] Yujia Li, David Choi, Junyoung Chung, Nate Kushman, Julian Schrittwieser, Rémi Leblond, Tom Eccles, James Keeling, Felix Gimeno, Agustin Dal Lago, et al. Competition-level code generation with alphacode. *Science*, 378(6624):1092–1097, 2022.
- [102] Shishir G Patil, Tianjun Zhang, Xin Wang, and Joseph E Gonzalez. Gorilla: Large language model connected with massive apis. *arXiv preprint arXiv:2305.15334*, 2023.
- [103] Jason Wei, Xuezhi Wang, Dale Schuurmans, Maarten Bosma, Fei Xia, Ed Chi, Quoc V Le, Denny Zhou, et al. Chain-of-thought prompting elicits reasoning in large language models. *Advances in neural information processing systems*, 35:24824–24837, 2022.
- [104] Jingqing Ruan, Yihong Chen, Bin Zhang, Zhiwei Xu, Tianpeng Bao, Hangyu Mao, Ziyue Li, Xingyu Zeng, Rui Zhao, et al. Tptu: Task planning and tool usage of large language model-based ai agents. In *NeurIPS 2023 Foundation Models for Decision Making Workshop*, 2023.
- [105] Zhibin Gou, Zhihong Shao, Yeyun Gong, Yujia Yang, Minlie Huang, Nan Duan, Weizhu Chen, et al. Tora: A tool-integrated reasoning agent for mathematical problem solving. *arXiv preprint arXiv:2309.17452*, 2023.
- [106] Tanmay Gupta and Aniruddha Kembhavi. Visual programming: Compositional visual reasoning without

- training. In *Proceedings of the IEEE/CVF Conference on Computer Vision and Pattern Recognition*, pages 14953–14962, 2023.
- [107] Sanjay Subramanian, Medhini Narasimhan, Kushal Khangaonkar, Kevin Yang, Arsha Nagrani, Cordelia Schmid, Andy Zeng, Trevor Darrell, and Dan Klein. Modular visual question answering via code generation. *arXiv preprint arXiv:2306.05392*, 2023.
- [108] Dídac Surís, Sachit Menon, and Carl Vondrick. Vipergpt: Visual inference via python execution for reasoning. In *Proceedings of the IEEE/CVF International Conference on Computer Vision*, pages 11888–11898, 2023.
- [109] Zhengyuan Yang, Linjie Li, Jianfeng Wang, Kevin Lin, Ehsan Azarnasab, Faisal Ahmed, Zicheng Liu, Ce Liu, Michael Zeng, and Lijuan Wang. Mm-react: Prompting chatgpt for multimodal reasoning and action. *arXiv preprint arXiv:2303.11381*, 2023.
- [110] Yifan Song, Weimin Xiong, Dawei Zhu, Wenhao Wu, Han Qian, Mingbo Song, Hailiang Huang, Cheng Li, Ke Wang, Rong Yao, et al. Restgpt: Connecting large language models with real-world restful apis. *arXiv preprint arXiv:2306.06624*, 2023.
- [111] Shunyu Yao, Howard Chen, John Yang, and Karthik Narasimhan. Webshop: Towards scalable real-world web interaction with grounded language agents. *Advances in Neural Information Processing Systems*, 35:20744–20757, 2022.
- [112] Xiang Deng, Yu Gu, Boyuan Zheng, Shijie Chen, Sam Stevens, Boshi Wang, Huan Sun, and Yu Su. Mind2web: Towards a generalist agent for the web. *Advances in Neural Information Processing Systems*, 36, 2024.
- [113] Andres M Bran, Sam Cox, Oliver Schilter, Carlo Baldassari, Andrew D White, and Philippe Schwaller. Chemcrow: Augmenting large-language models with chemistry tools. *arXiv preprint arXiv:2304.05376*, 2023.
- [114] Daniil A Boiko, Robert MacKnight, and Gabe Gomes. Emergent autonomous scientific research capabilities of large language models. *arXiv preprint arXiv:2304.05332*, 2023.
- [115] Yaobo Liang, Chenfei Wu, Ting Song, Wenshan Wu, Yan Xia, Yu Liu, Yang Ou, Shuai Lu, Lei Ji, Shaoguang Mao, et al. Taskmatrix. ai: Completing tasks by connecting foundation models with millions of apis. *Intelligent Computing*, 3:0063, 2024.
- [116] Yujia Qin, Shihao Liang, Yining Ye, Kunlun Zhu, Lan Yan, Yaxi Lu, Yankai Lin, Xin Cong, Xiangru Tang, Bill Qian, et al. Toolllm: Facilitating large language models to master 16000+ real-world apis. *arXiv preprint arXiv:2307.16789*, 2023.
- [117] Wenlong Huang, Fei Xia, Ted Xiao, Harris Chan, Jacky Liang, Pete Florence, Andy Zeng, Jonathan Tompson, Igor Mordatch, Yevgen Chebotar, et al. Inner monologue: Embodied reasoning through planning with language models. *arXiv preprint arXiv:2207.05608*, 2022.
- [118] Krishan Rana, Jesse Haviland, Sourav Garg, Jad Abou-Chakra, Ian Reid, and Niko Suenderhauf. Sayplan: Grounding large language models using 3d scene graphs for scalable task planning. *arXiv preprint arXiv:2307.06135*, 2023.
- [119] Zihao Wang, Shaofei Cai, Guanzhou Chen, Anji Liu, Xiaojian Ma, and Yitao Liang. Describe, explain, plan and select: Interactive planning with large language models enables open-world multi-task agents. *arXiv preprint arXiv:2302.01560*, 2023.
- [120] Guanzhi Wang, Yuqi Xie, Yunfan Jiang, Ajay Mandlekar, Chaowei Xiao, Yuke Zhu, Linxi Fan, and Anima Anandkumar. Voyager: An open-ended embodied agent with large language models. *arXiv preprint arXiv:2305.16291*, 2023.
- [121] Shunyu Yao, Jeffrey Zhao, Dian Yu, Nan Du, Izhak Shafran, Karthik Narasimhan, and Yuan Cao. React: Synthesizing reasoning and acting in language models. *arXiv preprint arXiv:2210.03629*, 2022.
- [122] Xizhou Zhu, Yuntao Chen, Hao Tian, Chenxin Tao, Weijie Su, Chenyu Yang, Gao Huang, Bin Li, Lewei Lu, Xiaogang Wang, et al. Ghost in the minecraft: Generally capable agents for open-world environments via large language models with text-based knowledge and memory. *arXiv preprint arXiv:2305.17144*, 2023.
- [123] Binxu Li, Tiankai Yan, Yuanting Pan, Zhe Xu, Jie Luo, Ruiyang Ji, Shilong Liu, Haoyu Dong, Zihao Lin, and Yixin Wang. Mmedagent: Learning to use medical tools with multi-modal agent. *arXiv preprint arXiv:2407.02483*, 2024.
- [124] Fausto Milletari, Nassir Navab, and Seyed-Ahmad Ahmadi. V-net: Fully convolutional neural networks for volumetric medical image segmentation. In *2016 fourth international conference on 3D vision (3DV)*, pages 565–571. Ieee, 2016.
- [125] Adam Paszke, Sam Gross, Francisco Massa, Adam Lerer, James Bradbury, Gregory Chanan, Trevor Killeen, Zeming Lin, Natalia Gimelshein, Luca Antiga, et al. Pytorch: An imperative style, high-performance deep learning library. *Advances in neural information processing systems*, 32, 2019.
- [126] Hugo Touvron, Louis Martin, Kevin Stone, Peter Albert, Amjad Almahairi, Yasmine Babaei, Nikolay Bashlykov, Soumya Batra, Prajjwal Bhargava, Shruti Bhosale, et al. Llama 2: Open foundation and fine-tuned chat models. *arXiv preprint arXiv:2307.09288*, 2023.
- [127] Thomas Wolf, Lysandre Debut, Victor Sanh, Julien Chaumond, Clement Delangue, Anthony Moi, Pierric Cistac, Tim Rault, Rémi Louf, Morgan Funtowicz, et al. Huggingface’s transformers: State-of-the-art natural language processing. *arXiv preprint arXiv:1910.03771*, 2019.
- [128] Olaf Ronneberger, Philipp Fischer, and Thomas Brox. U-net: Convolutional networks for biomedical image segmentation. In *Medical image computing and computer-assisted intervention—MICCAI 2015: 18th international conference, Munich, Germany, October 5-9, 2015, proceedings, part III 18*, pages 234–241. Springer, 2015.

- [129] Diederik P Kingma and Jimmy Ba. Adam: A method for stochastic optimization. *arXiv preprint arXiv:1412.6980*, 2014.
- [130] Daniel S Marcus, Tracy H Wang, Jamie Parker, John G Csernansky, John C Morris, and Randy L Buckner. Open access series of imaging studies (oasis): cross-sectional mri data in young, middle aged, nondemented, and demented older adults. *Journal of cognitive neuroscience*, 19(9):1498–1507, 2007.
- [131] Pamela J LaMontagne, Tammie LS Benzinger, John C Morris, Sarah Keefe, Russ Hornbeck, Chengjie Xiong, Elizabeth Grant, Jason Hassenstab, Krista Moulder, Andrei G Vlassenko, et al. Oasis-3: longitudinal neuroimaging, clinical, and cognitive dataset for normal aging and alzheimer disease. *MedRxiv*, pages 2019–12, 2019.
- [132] Anahit Babayan, Miray Erbey, Deniz Kumral, Janis D Reinelt, Andrea MF Reiter, Josefin Röbbig, H Lina Schaare, Marie Uhlig, Alfred Anwander, Pierre-Louis Bazin, et al. A mind-brain-body dataset of mri, eeg, cognition, emotion, and peripheral physiology in young and old adults. *Scientific data*, 6(1):1–21, 2019.
- [133] Ana Luísa Pinho, Alexis Amadon, Torsten Ruest, Murielle Fabre, Elvis Dohmatob, Isabelle DENGHIEN, Chantal GINISTY, Séverine Becuwe-Desmidt, Séverine Roger, Laurence Laurier, et al. Individual brain charting, a high-resolution fmri dataset for cognitive mapping. *Scientific data*, 5(1):1–15, 2018.
- [134] Inés Mérida, Julien Jung, Sandrine Bouvard, Didier Le Bars, Sophie Lancelot, Franck Lavenne, Caroline Bouillot, Jérôme Redouté, Alexander Hammers, and Nicolas Costes. Cermep-idb-mrxfdg: A database of 37 normal adult human brain [18f] fdg pet, t1 and flair mri, and ct images available for research. *EJNMMI research*, 11(1):1–10, 2021.
- [135] Michael Hanke, Florian J Baumgartner, Pierre Ibe, Falko R Kaule, Stefan Pollmann, Oliver Speck, Wolf Zinke, and Jörg Stadler. A high-resolution 7-tesla fmri dataset from complex natural stimulation with an audio movie. *Scientific data*, 1(1):1–18, 2014.
- [136] Andrew Hoopes, Jocelyn S Mora, Adrian V Dalca, Bruce Fischl, and Malte Hoffmann. Synthstrip: Skull-stripping for any brain image. *NeuroImage*, 260:119474, 2022.
- [137] Syed M Adil, Evan Calabrese, Lefko T Charalambous, James J Cook, Shervin Rahimpour, Ahmet F Atik, Gary P Cofer, Beth A Parente, G Allan Johnson, Shivanand P Lad, et al. A high-resolution interactive atlas of the human brainstem using magnetic resonance imaging. *Neuroimaging*, 237:118135, 2021.
- [138] Wolfgang M Pauli, Amanda N Nili, and J Michael Tyszka. A high-resolution probabilistic in vivo atlas of human subcortical brain nuclei. *Scientific data*, 5(1):1–13, 2018.
- [139] Moritz R Hernandez Petzsche, Ezequiel de la Rosa, Uta Hanning, Roland Wiest, Waldo Valenzuela, Mauricio Reyes, Maria Meyer, Sook-Lei Liew, Florian Kofler, Ivan Ezhov, et al. Isles 2022: A multi-center magnetic resonance imaging stroke lesion segmentation dataset. *Scientific data*, 9(1):762, 2022.
- [140] Sook-Lei Liew, Bethany P Lo, Miranda R Donnelly, Artemis Zavaliangos-Petropulu, Jessica N Jeong, Giuseppe Barisano, Alexandre Hutton, Julia P Simon, Julia M Juliano, Anisha Suri, et al. A large, curated, open-source stroke neuroimaging dataset to improve lesion segmentation algorithms. *Scientific data*, 9(1):320, 2022.
- [141] Malte Hoffmann, Andrew Hoopes, Douglas N. Greve, Bruce Fischl, and Adrian V. Dalca. Anatomy-aware and acquisition-agnostic joint registration with SynthMorph. *Imaging Neuroscience*, 2:1–33, 06 2024. ISSN 2837-6056. doi: 10.1162/imag_a_00197.
- [142] Lee R Dice. Measures of the amount of ecologic association between species. *Ecology*, 26(3):297–302, 1945.
- [143] Josh Achiam, Steven Adler, Sandhini Agarwal, Lama Ahmad, Ilge Akkaya, Florencia Leoni Aleman, Diogo Almeida, Janko Altenschmidt, Sam Altman, Shyamal Anadkat, et al. Gpt-4 technical report. *arXiv preprint arXiv:2303.08774*, 2023.

Appendix

A.1 Native-Space Convolutions

Volumetric image formats typically include a world coordinate transform that defines the in-plane voxel spacing (s^{inp}) and the spacing between slices (s^{sep}). We define the relative slice-to-in-plane spacing as $\omega = s^{sep}/s^{inp}$. Standard image processing methods resample inputs to a common, often isotropic resolution (i.e., $\omega = 1$). However, this can remove signal of high-resolution scans or unnecessarily increase data density of thick-slice acquisitions.

To address this, we implement resolution-agnostic convolutional layers that process volumes in their native voxel spacing. Throughout the multi-scale vision network, we track and recompute voxel spacings. In the downsampling operation following resolution level n , images are resampled to the following spacing:

$$s_{n+1}^{inp} = 2 s_n^{inp}, \quad s_{n+1}^{sep} = \begin{cases} s^{sep} & \text{if } \omega_n > 2, \\ s_{n+1}^{inp} & \text{otherwise.} \end{cases}$$

During upsampling, this process is reversed. To prevent disproportionate convolution of spatial information for volumes with $\omega_n > 2$, we instead apply a 2D convolution across each volume slice, using a central 3D kernel slice extracted from the image through-plane dimension.

A.2 List of Anatomical Structures

We use segmentations of various anatomical classes, listed below. Bilateral brain structures are defined by two distinct hemisphere-specific labels.

Global tissue classes include the brain, dura, skull cavity, cerebrum, cerebral white matter, cerebral cortex, brainstem, cerebellum, ventricular system, and cerebral spinal fluid (CSF). Brain sub-structure labels include the amygdala, nucleus accumbens, hippocampus, thalamus, caudate, putamen, dorsal striatum, globus pallidus (externus and internus), basal ganglia, hypothalamus, fornix (body, crus, and column), mammillary body, septal nucleus, subthalamic nucleus, habenula, ventral pallidum, extended amygdala, red nucleus, anterior and posterior commissures, pars compacta, pars reticulata, parabrachial pigmented nucleus, ventral tegmental area, fimbria, septum pellucidum, tectum, pineal gland, superior and inferior colliculus, cerebral peduncle, medullary pyramid, medial lemniscus, superior cerebellar peduncle, middle cerebellar peduncle, inferior cerebellar peduncle, cerebellar gray matter, and cerebellar white matter. Ventricular sub-structure labels include the lateral ventricle, inferior lateral ventricle, posterior lateral ventricle, anterior lateral ventricle, atrium, third ventricle, fourth ventricle, inter-ventricular foramen, and cerebral aqueduct.

Cortical sub-region labels include the frontal lobe, parietal lobe, temporal lobe, occipital lobe, cingulate cor-

tex, insular cortex, anterior cingulate cortex, caudal anterior cingulate cortex, rostral anterior cingulate cortex, posterior cingulate cortex, isthmus cingulate cortex, frontal pole, middle frontal gyrus, caudal middle frontal gyrus, rostral middle frontal gyrus, superior frontal gyrus, inferior frontal gyrus, pars opercularis, pars orbitalis, pars triangularis, lateral orbitofrontal cortex, medial orbitofrontal cortex, precentral gyrus, paracentral lobule, inferior parietal lobule, superior parietal lobule, supramarginal gyrus, precuneus, postcentral gyrus, entorhinal cortex, fusiform gyrus, parahippocampal gyrus, temporal pole, inferior temporal gyrus, middle temporal gyrus, superior temporal gyrus, transverse temporal gyrus, cuneus, lingual gyrus, and pericalcarine cortex.

A.3 Lesion Synthesis

We broaden the diversity of pathological image features in training by synthesizing brain abnormalities with variable traits. We implement a model-based domain randomization technique to augment images from healthy patients.

To create a random lesion during training, we first choose a target anatomical location and define a lesion boundary radius. A spherical boundary of the chosen radius is then sampled within a segmentation corresponding to the target anatomy. Inside this boundary, we generate multiple ellipsoids with random positions, rotations, and sizes, which are combined and further modified using random dilation, erosion, and non-linear deformation to produce the final lesion mask.

The lesion mask is in-painted into scans of a sampled subject. For each scan, we decide whether the lesion will appear hyperintense, hypointense, or isointense, and assign a random fill intensity relative to the surrounding tissue. To simulate heterogeneous intensities, a secondary lesion geometry is superimposed on the original mask.

A.4 Segmentation Analysis Data

In the table below, we summarize the number of unique images and subjects used to evaluate each label in the segmentation analysis (Section 5.2). All evaluations that involve an *anatomical* label use the same set of evaluation images, so we group them together below.

Segmentation Target	Images	Subjects
infarct	206	206
glioma	1,376	344
edema	1,386	347
cyst	24	11
papilloma	16	6
meningioma	21	8
white matter hyperintensities	40	20
anatomical structure	108	40

A.5 Classification Analysis Data

In the table below, we summarize the number of unique images and subjects used to evaluate each task in the pathology characterization analysis (Section 5.3).

Classification Task	Images	Subjects
characterize lesion signal intensity	26	26
identify lesion cerebral location	112	30
identify infarct vascular territory	16	12
detect diffusion restriction	28	14
detect post-contrast enhancement	40	20

A.6 Zero-Shot Baseline Evaluation

We assess the zero-shot performance of RadFM [77] and ChatGPT-4o [143] on the subset of pathology characterization tasks used in Section 5.3. For each test sample, we provide these models with a detailed task description and all available images. To ensure a fair comparison, we include additional context in the input prompt, along with a set of possible answers for each question. The input prompts used for each task category are detailed below:

- Given the following brain scan(s), classify the lesion signal intensity as either hyperintense or hypointense.
- Given the following brain scan(s), classify the lesion location as either the temporal lobe, frontal lobe, parietal lobe, brainstem, or cerebellum.
- Given the following brain scan(s), classify the infarct location as either the ACA, MCA, or PCA territory.
- Given the following DWI and ADC brain scans, classify the lesion as diffusion restricting or non-restricting.
- Given the following pre- and post-contrast brain scans, indicate if the lesion is contrast enhancing.

RadFM Zero-Shot Evaluation. To match RadFM input constraints, we resample all image shapes to multiples of $32 \times 32 \times 4$. For each test case, we run evaluations across all possible voxel orientations of the volume data and run additional tests with the volume depth resampled to 64 voxels – the maximum depth used in RadFM pretraining.

ChatGPT Zero-Shot Evaluation. ChatGPT-4o is primarily designed for 2D image inputs rather than volumetric data. Thus, we convert each 3D volume into multi-plane cross-sectional slices centered on the relevant region of interest. Note that this slicing method biases ChatGPT predictions by effectively pinpointing the lesion location within the full volume.

Results. Across all characterization tasks, RadFM fails to correctly classify *any* test sample, and ChatGPT achieves an average accuracy of only $58.6 \pm 14.1\%$, suggesting an inability to generalize to complex medical imaging tasks.

A.7 Radiopaedia Data

We download the following patient cases from Radiopaedia, a radiology reference website at <https://radiopaedia.org>. Each case includes text-based notes and brain scans in the form of 2D image slices. We reconstruct volumetric data by stacking these slices and estimating an affine matrix to map voxel coordinates in world space. We compute this mapping by registering the image to an average brain template with SynthMorph [141].

Case References

- Abdelmonem H, Suprasellar arachnoid cyst.
<https://doi.org/10.53347/rID-50712>
- Abdrabou A, Central neurocytoma.
<https://doi.org/10.53347/rID-67618>
- Abdrabou A, Fungal cerebral abscesses.
<https://doi.org/10.53347/rID-34829>
- Abdrabou A, Intracranial epidermoid cyst.
<https://doi.org/10.53347/rID-41892>
- Abdrabou A, Meningioma - cerebellopontine angle.
<https://doi.org/10.53347/rID-36505>
- Abdrabou A, Pancoast tumor with cystic cerebral metastasis.
<https://doi.org/10.53347/rID-27303>
- Al Ja'afreh H, Meningioma.
<https://doi.org/10.53347/rID-174815>
- Al Khateeb A, Meningioma.
<https://doi.org/10.53347/rID-43429>
- Al Khateeb A, Suprasellar arachnoid cyst.
<https://doi.org/10.53347/rID-45162>
- Al Salam H, Arachnoid cyst.
<https://doi.org/10.53347/rID-10869>
- Al Salam H, Central neurocytoma.
<https://doi.org/10.53347/rID-9589>
- Al Salam H, Choroid plexus papilloma.
<https://doi.org/10.53347/rID-8466>
- Alghamdi K, Intracranial epidermoid cyst.
<https://doi.org/10.53347/rID-78159>
- Almoghazy S, Intracranial epidermoid cyst.
<https://doi.org/10.53347/rID-86783>
- Amer M, Central neurocytoma.
<https://doi.org/10.53347/rID-184648>
- Asadov D, Meningioma.
<https://doi.org/10.53347/rID-8837>
- Babu V, Arachnoid cyst.
<https://doi.org/10.53347/rID-46791>
- Balachandran G, Posterior fossa meningioma.
<https://doi.org/10.53347/rID-5597>
- Bayat M, Choroid plexus papilloma.
<https://doi.org/10.53347/rID-76732>
- Ben-Shabat E, Stroke progression.
<https://doi.org/10.53347/rID-93012>
- Bickle I, Intraventricular meningioma.
<https://doi.org/10.53347/rID-45529>

- Bickle I, Multicentric glioblastoma.
<https://doi.org/10.53347/rID-88861>
- Bickle I, Petrous ridge meningioma.
<https://doi.org/10.53347/rID-50777>
- Bickle I, Subacute subdural hematoma.
<https://doi.org/10.53347/rID-32123>
- Bickle I, Suprasellar arachnoid cyst - pediatric.
<https://doi.org/10.53347/rID-82691>
- Cuete D, Mega cisterna magna.
<https://doi.org/10.53347/rID-26363>
- Cuete D, Meningioma.
<https://doi.org/10.53347/rID-22919>
- Desai P, Frontal meningioma.
<https://doi.org/10.53347/rID-19463>
- Di Muzio B, Brain metastasis (large cystic mass).
<https://doi.org/10.53347/rID-47497>
- Di Muzio B, Falcine meningioma.
<https://doi.org/10.53347/rID-40869>
- Ebouda F, Left occipital late subacute epidural hematoma.
<https://doi.org/10.53347/rID-28001>
- Elfeky M, Arachnoid cyst.
<https://doi.org/10.53347/rID-42196>
- Elfeky M, Cerebral convexity epidermoid.
<https://doi.org/10.53347/rID-43105>
- Farhadi M, Arachnoid cyst - bilateral middle cranial fossa.
<https://doi.org/10.53347/rID-183101>
- Farzam F, Epidermoid cyst - middle cranial fossa.
<https://doi.org/10.53347/rID-69937>
- Gaillard F, Arachnoid cyst - cerebellopontine angle.
<https://doi.org/10.53347/rID-8219>
- Gaillard F, Arachnoid cyst - posterior fossa.
<https://doi.org/10.53347/rID-4544>
- Gaillard F, Arachnoid cyst - suprasellar.
<https://doi.org/10.53347/rID-8914>
- Gaillard F, Cavum velum interpositum cyst.
<https://doi.org/10.53347/rID-15981>
- Gaillard F, Central neurocytoma.
<https://doi.org/10.53347/rID-21041>
- Gaillard F, Central neurocytoma.
<https://doi.org/10.53347/rID-33049>
- Gaillard F, Central neurocytoma.
<https://doi.org/10.53347/rID-4002>
- Gaillard F, Central neurocytoma.
<https://doi.org/10.53347/rID-65317>
- Gaillard F, Choroid plexus papilloma.
<https://doi.org/10.53347/rID-33040>
- Gaillard F, Encephalomalacia.
<https://doi.org/10.53347/rID-22285>
- Gaillard F, Epidermoid cyst (cerebellopontine angle).
<https://doi.org/10.53347/rID-33762>
- Gaillard F, Epidermoid cyst - suprasellar.
<https://doi.org/10.53347/rID-16839>
- Gaillard F, Epidermoid cyst: frontal and cerebellopontine angle.
<https://doi.org/10.53347/rID-58135>
- Gaillard F, Glioblastoma, IDH- wildtype (pseudoprogression).
<https://doi.org/10.53347/rID-42209>
- Gaillard F, Olfactory groove meningioma - huge.
<https://doi.org/10.53347/rID-31075>
- Gaillard F, Pineal epidermoid cyst.
<https://doi.org/10.53347/rID-99497>
- Gaillard F, Suprasellar arachnoid cyst - massive.
<https://doi.org/10.53347/rID-62759>
- Gaillard F, Suprasellar arachnoid cyst.
<https://doi.org/10.53347/rID-75082>
- Geetha Virupakshappa A, Arachnoid cyst - Galassi type III.
<https://doi.org/10.53347/rID-149904>
- Gewolb D, Arachnoid cyst - intracystic hemorrhage.
<https://doi.org/10.53347/rID-161492>
- Goel A, Hemorrhagic cerebral metastases.
<https://doi.org/10.53347/rID-26687>
- Hamidi H, Meningioma.
<https://doi.org/10.53347/rID-50810>
- Haouimi A, Arachnoid cyst - middle cranial fossa.
<https://doi.org/10.53347/rID-85061>
- Haouimi A, Arachnoid cyst - sellar and suprasellar.
<https://doi.org/10.53347/rID-96728>
- Haouimi A, Meningioma - frontal convexity.
<https://doi.org/10.53347/rID-79485>
- Haouimi A, Subependymal heterotopia - cyst of the velum interpositum.
<https://doi.org/10.53347/rID-74488>
- Haouimi A, Suprasellar arachnoid cyst.
<https://doi.org/10.53347/rID-99076>
- Hartung M, Acute on chronic subdural hematoma.
<https://doi.org/10.53347/rID-78346>
- Hospital R, Epidermoid cyst.
<https://doi.org/10.53347/rID-13721>
- Hosseinabadi F, Suprasellar arachnoid cyst.
<https://doi.org/10.53347/rID-74656>
- Husen H, Choroid plexus papilloma.
<https://doi.org/10.53347/rID-89256>
- Kabra U, Cerebral abscess.
<https://doi.org/10.53347/rID-157965>
- Kabra U, Choroid plexus papilloma.
<https://doi.org/10.53347/rID-84612>
- Knipe H, Meningioma.
<https://doi.org/10.53347/rID-56937>
- Mahmoud Q, Brain metastases from breast cancer.
<https://doi.org/10.53347/rID-164146>
- Mahmoud Q, Meningioma.
<https://doi.org/10.53347/rID-183767>
- Marghany B, Epidermoid cyst.
<https://doi.org/10.53347/rID-67246>
- Mishra H, Meningioma.
<https://doi.org/10.53347/rID-90656>
- Mudgal P, Bilateral sub-acute subdural hematomas.
<https://doi.org/10.53347/rID-27476>
- Mudgal P, Central neurocytoma.
<https://doi.org/10.53347/rID-30220>

Mudgal P, Intracranial epidermoid cyst - cerebellopontine angle.
<https://doi.org/10.53347/rID-26565>

Neto A, Arachnoid cyst - middle cranial fossa.
<https://doi.org/10.53347/rID-71674>

Neuropathology R, Central neurocytoma.
<https://doi.org/10.53347/rID-37664>

Neuropathology R, Choroid plexus papilloma and acoustic scwhannoma.
<https://doi.org/10.53347/rID-28131>

Neuropathology R, Choroid plexus papilloma.
<https://doi.org/10.53347/rID-38522>

Niknejad M, Epidermoid cyst - cerebellopontine angle.
<https://doi.org/10.53347/rID-61773>

Osman M, Chordoid meningioma.
<https://doi.org/10.53347/rID-23037>

Perera A, Choroid plexus papilloma.
<https://doi.org/10.53347/rID-92022>

Pirzad F, Arachnoid cyst.
<https://doi.org/10.53347/rID-9619>

Pirzad F, Cerebellar hemorrhage.
<https://doi.org/10.53347/rID-9620>

Qureshi P, Meningioma.
<https://doi.org/10.53347/rID-69335>

Ranchod A, Intracranial epidermoid cyst.
<https://doi.org/10.53347/rID-94043>

Ranchod A, Planum sphenoidale meningioma.
<https://doi.org/10.53347/rID-97514>

Rasuli B, Epidermoid cyst - cerebellopontine angle.
<https://doi.org/10.53347/rID-83470>

Rasuli B, Intracranial epidermoid cyst.
<https://doi.org/10.53347/rID-170531>

Saber M, Cavum velum interpositum cyst.
<https://doi.org/10.53347/rID-155458>

Saber M, Early and late subacute intracerebral hemorrhage.
<https://doi.org/10.53347/rID-148791>

Schubert R, Cavum velum interpositum cyst.
<https://doi.org/10.53347/rID-13825>

Sorrentino S, Arachnoid cyst.
<https://doi.org/10.53347/rID-19826>

Sorrentino S, Convexity meningioma.
<https://doi.org/10.53347/rID-16004>

Stanislavsky A, Central neurocytoma.
<https://doi.org/10.53347/rID-13188>

Tarasov N, Intracranial epidermoid cyst - posterior fossa.
<https://doi.org/10.53347/rID-39109>

Thapa S, Arachnoid cyst - Galassi type III.
<https://doi.org/10.53347/rID-40204>

Thibodeau R, Choroid plexus papilloma.
<https://doi.org/10.53347/rID-166392>

Trajcevska E, Suprasellar arachnoid cyst.
<https://doi.org/10.53347/rID-22877>

Voss Y, Hyperacute intracerebral hemorrhage.
<https://doi.org/10.53347/rID-49757>